

Mitochondrial translation requires folate-dependent tRNA methylation

Raphael J. Morscher^{1,2}, Gregory S. Ducker^{1,2}, Sophia Hsin-Jung Li³, Johannes A. Mayer⁴, Zemer Gitai³, Wolfgang Sperl⁴ & Joshua D. Rabinowitz^{1,2}

Folates enable the activation and transfer of one-carbon units for the biosynthesis of purines, thymidine and methionine^{1–3}. Antifolates are important immunosuppressive⁴ and anticancer agents⁵. In proliferating lymphocytes⁶ and human cancers^{7,8}, mitochondrial folate enzymes are particularly strongly upregulated. This in part reflects the need for mitochondria to generate one-carbon units and export them to the cytosol for anabolic metabolism^{2,9}. The full range of uses of folate-bound one-carbon units in the mitochondrial compartment itself, however, has not been thoroughly explored. Here we show that loss of the catalytic activity of the mitochondrial folate enzyme serine hydroxymethyltransferase 2 (SHMT2), but not of other folate enzymes, leads to defective oxidative phosphorylation in human cells due to impaired mitochondrial translation. We find that SHMT2, presumably by generating mitochondrial 5,10-methylenetetrahydrofolate, provides methyl donors to produce the taurinomethyluridine base at the wobble position of select mitochondrial tRNAs. Mitochondrial ribosome profiling in SHMT2-knockout human cells reveals that the lack of this modified base causes defective translation, with preferential mitochondrial ribosome stalling at certain lysine (AAG) and leucine (UUG) codons. This results in the impaired expression of respiratory chain enzymes. Stalling at these specific codons also occurs in certain inborn errors of mitochondrial metabolism. Disruption of whole-cell folate metabolism, by either folate deficiency or antifolate treatment, also impairs the respiratory chain. In summary, mammalian mitochondria use folate-bound one-carbon units to methylate tRNA, and this modification is required for mitochondrial translation and thus oxidative phosphorylation.

The major source of folate one-carbon (1C) units in mammalian cells is the amino acid serine^{1–3}. Transfer of the 1C unit of serine to tetrahydrofolate (THF) can occur in either the cytosol or the mitochondrion, via the enzyme SHMT1 or SHMT2, respectively¹⁰ (Fig. 1a). Evidence from stable isotope tracing indicates that cancer cells predominantly use SHMT2 to catabolize serine, exporting the resulting 1C units to the cytosol to support nucleotide synthesis^{2,9}. The extent to which 1C unit production via SHMT2 is also important to support mitochondrial health has yet to be determined.

When characterizing a set of human HCT116 colon cancer CRISPR-deletion cell lines that lack folate 1C enzymes, we discovered that the loss of SHMT2 induces a change in media colour indicative of enhanced extracellular acidification (Extended Data Fig. 1a). Quantitative analysis of the media confirmed increased glucose uptake and lactate secretion. This effect was specific to SHMT2: loss of other core 1C enzymes, including SHMT1 and mitochondrial enzymes such as MTHFD2 and MTHFD1L, did not induce glycolysis (Fig. 1b, Extended Data Fig. 1b).

A common cause of increased glycolytic flux is respiratory deficiency¹¹. Loss of SHMT2 reduced both basal respiration and

maximal respiratory capacity and decreased the NAD⁺/NADH ratio in several HCT116 (Fig. 1c, Extended Data Fig. 1c) and HEK293T SHMT2-knockout clones. Knockout cell lines lacking other core folate enzymes did not show impaired respiration (Extended Data Fig. 1d, e). Consistent with respiratory chain deficiency, the loss of SHMT2 decreased glucose flux into the tricarboxylic acid (TCA) cycle intermediate citrate, with an increased fraction of citrate instead being produced by reductive carboxylation¹². As reported recently in other models of mitochondrial damage^{13,14}, the pool size of TCA cycle metabolites and associated amino acids was also decreased (Extended Data Fig. 1f, g). To identify the cause of respiratory deficiency, we examined the abundances of several mitochondrial proteins, and found decreased abundances of complex I, IV and V subunits with retained levels of complexes II and III and markers of mitochondrial mass (Fig. 1d and Extended Data Fig. 1h, i). Thus, SHMT2 is required to maintain the levels of several mitochondrial respiratory chain proteins.

Given that the loss of SHMT2, but not of the immediate downstream enzymes of mitochondrial 1C metabolism, caused impaired oxidative phosphorylation, we wondered whether the phenotype reflected a requirement for the catalytic activity of SHMT2, or alternatively a non-catalytic role of SHMT2, perhaps related to its reported interaction with the mitochondrial nucleoid¹⁵. Accordingly, in the SHMT2-knockout background, we stably re-expressed catalytically inactive SHMT2 (p.Glu98Leu/p.Tyr106Phe), pyridoxal 5'-phosphate (PLP)-binding mutant SHMT2 (p.Lys280Gln) or wild-type SHMT2 protein (Extended Data Figs 2, 3a). Re-expression of wild-type protein, but not the catalytically inactive mutants, rescued the oxidative phosphorylation deficiency (Fig. 1e and Extended Data Fig. 3b) and normalized glycolytic flux (Extended Data Fig. 3c). In addition, SHMT2 re-expression rescued the growth defect of SHMT2-knockout cells⁹ (Extended Data Fig. 3d) and normalized 1C metabolism (Extended Data Fig. 3e, f). Thus, mitochondrial SHMT catalytic activity is crucial to sustain oxidative phosphorylation.

Two compartment-specific uses of mitochondrial folate 1C units have been reported: the local biosynthesis of deoxythymidine triphosphate (dTTP)^{16,17} and of *N*-formylmethionine (*f*-Met)^{18,19} (Fig. 2a). The production of dTTP requires 5,10-methylene-THF (methylene-THF), whereas *f*-Met requires 10-formyl-THF (formyl-THF). SHMT2 is upstream of both compounds. By contrast, MTHFD2 sits between methylene-THF and formyl-THF. The lack of an oxidative phosphorylation phenotype with MTHFD2 knockout led us to hypothesize that methylene-THF is the required 1C species. Consistent with this, SHMT2-knockout cell lines showed unchanged N-terminal *f*-Met levels of the mitochondrially translated COX1 peptide (encoded by the *MT-CO1* gene)¹⁹ (Extended Data Fig. 4a). To confirm that methylene-THF is the required species, we generated SHMT2/MTHFD2 double-deletion cells and supplemented them with methylglycine (sarcosine), which can produce mitochondrial methylene-THF

¹Lewis-Sigler Institute for Integrative Genomics, Princeton University, Princeton, New Jersey 08544, USA. ²Department of Chemistry, Princeton University, Princeton, New Jersey 08544, USA.

³Department of Molecular Biology, Princeton University, Princeton, New Jersey 08544, USA. ⁴Department of Pediatrics, Salzburger Landeskliniken and Paracelsus Medical University, Salzburg 5020, Austria.

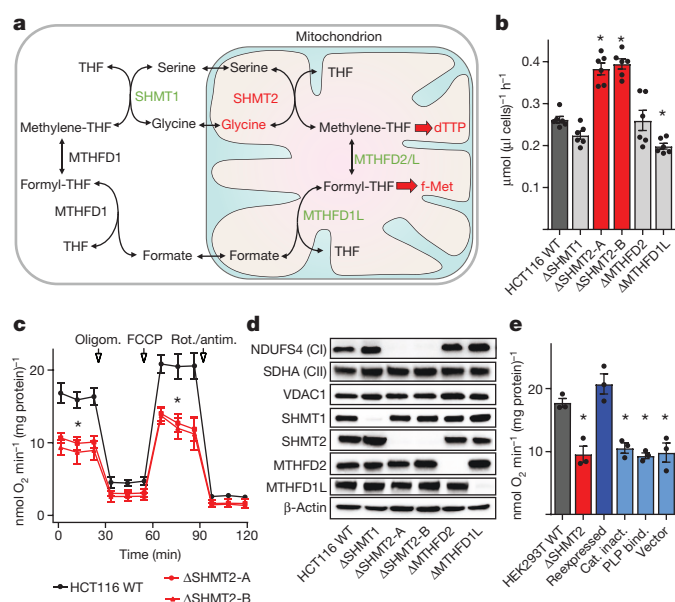


Figure 1 | Mitochondrial respiratory chain function is dependent on SHMT2 catalytic activity. **a**, 1C pathway and known mitochondrial products. **b**, Lactate secretion of HCT116-knockout cell lines ($n = 6$). Δ SHMT2-A and Δ SHMT2-B denote two separate SHMT2-knockout lines. WT, wild type. **c**, Oxygen consumption rate measured by Seahorse XF analyser ($n = 3$). FCCP denotes a mitochondrial uncoupling agent. Oligom., oligomycin; Rot./antim., rotenone/antimycin. **d**, Immunoblot for mitochondrial respiratory complex I and II (CI and CII) proteins (NDUFS4 and SDHA, respectively), 1C enzymes, and a marker of mitochondrial mass (VDAC1). **e**, Basal respiration ($n = 3$) upon re-expression of wild-type or catalytically deficient mutant forms of SHMT2 in HEK293T knockout cell lines. Data are mean \pm s.e.m. n indicates the number of biological replicates, which for the Seahorse experiments refers to independent plates on separate days. * $P < 0.01$, two-tailed Student's t -test (see Supplementary Table 7 for exact P values). Cat. inact., catalytically inactive SHMT2; PLP bind., PLP binding-deficient SHMT2.

via sarcosine dehydrogenase. Although sarcosine is not a preferred 1C source and its feeding was insufficient to restore oxidative phosphorylation in SHMT2 single gene knockout cell lines, it fully restored oxidative phosphorylation in the SHMT2/MTHFD2 double-knockout cells,

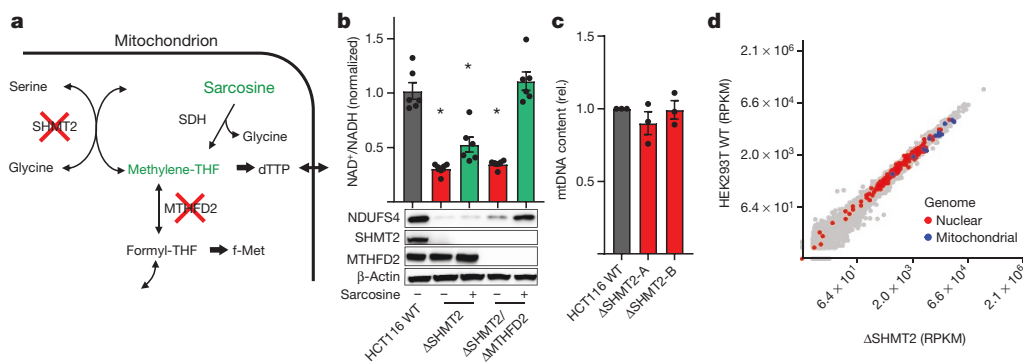


Figure 2 | SHMT2-knockout-induced respiratory chain deficiency is caused by mitochondrial methylene-THF depletion but is unrelated to dTTP synthesis. **a**, Sarcosine serves as an SHMT2-independent source of mitochondrial methylene-THF. **b**, NAD^+/NADH ratio ($n = 6$) and NDUFS4 (complex I) protein expression upon sarcosine supplementation (1 mM) in SHMT2 single-knockout (Δ SHMT2) and SHMT2/MTHFD2 double-knockout (Δ SHMT2/ Δ MTHFD2) cell lines compared to wild-type cells. **c**, **d**, Functional readouts for mitochondrial dTTP status based on mitochondrial DNA (mtDNA) levels ($n = 3$) determined by quantitative PCR (qPCR; **c**) and gene expression determined by

in which drainage of methylene-THF to formyl-THF is blocked (Fig. 2b and Extended Data Fig. 4b). Thus, mitochondrial methylene-THF is required to maintain respiratory capacity.

Depletion of mitochondrial dTTP and/or accumulation of uridine nucleotides have been shown to induce mitochondrial respiratory chain deficiency by promoting mitochondrial DNA damage^{17,20}. However, SHMT2-knockout cells showed no evidence of altered mitochondrial DNA copy number (Fig. 2c and Extended Data Fig. 4c), deletions (Extended Data Fig. 4d), or mutations (Extended Data Fig. 4g, h and Supplementary Table 1). Moreover, whole-cell RNA sequencing revealed normal transcript levels for both nuclear and mitochondrial-encoded respiratory chain protein subunits (Fig. 2d, Extended Data Fig. 4e, f). Thus, the dependence of oxidative phosphorylation on SHMT2 reflects a requirement for mitochondrial methylene-THF for a purpose other than supplying local dTTP to maintain mitochondrial DNA.

Whereas the vast majority of the approximately 1,100 mitochondrial proteins are imported from the cytosol, 13 essential respiratory chain subunits are locally transcribed and translated²¹. These include components of complexes I, III, IV and V, but not complex II. On the basis of the normal mitochondrial transcript abundances and complex II protein levels, we hypothesized that mitochondrial methylene-THF is required for local translation. Indeed, [³⁵S]methionine incorporation assays showed decreased synthesis of certain complex I and IV subunits (Extended Data Fig. 5a). To probe mitochondrial translation further, we developed a protocol for mitochondrial ribosome profiling based on digesting unprotected mRNA with micrococcal nuclease, enriching the 55S mitochondrial ribosome, and sequencing the protected footprints (Fig. 3a and Extended Data Fig. 5b). This approach achieved more than 90% average mitochondrial transcript sequence coverage, with an average depth of at least 80 reads per codon (Supplementary Table 3 and Extended Data Fig. 5c). In SHMT2-knockout cells, the distribution of ribosome-protected footprints showed pronounced stalling at defined codon positions (Fig. 3b and Extended Data Fig. 6a). This resulted in relatively fewer actively translating ribosomes (that is, bound and not stalled) for certain subunits of respiratory chain complexes I, IV and V (Extended Data Fig. 6b). Consistent with the ribosome profiling data, enzymatic assays revealed decreased activity of complexes I, IV and V (Extended Data Fig. 6c).

We next aimed to determine the cause of ribosomal stalling. The aminoacyl-tRNA acceptor-site (A-site) coordinates of stalled ribosomes revealed notable ribosome accumulation in SHMT2-knockout cells at particular lysine and leucine codons: Lys^{AAG} and Leu^{UUG} (Fig. 3c).

RNA-seq (**d**) in SHMT2-knockout and wild-type HEK293T cells. RPKM, reads per kilobase per million mapped reads. In **d**, each data point represents the mean gene expression of two biological replicates of two independent knockout clones ($n = 4$) and two wild-type replicates ($n = 2$). Genes linked to OXPHOS function³⁷ are highlighted in red (nuclear-encoded) or blue (mitochondrial-encoded). Significantly differentially expressed genes are shown in Supplementary Table 2. Data are mean \pm s.e.m. n indicates the number of independent biological replicates. * $P < 0.01$, two-tailed Student's t -test (see Supplementary Table 7 for exact P values).

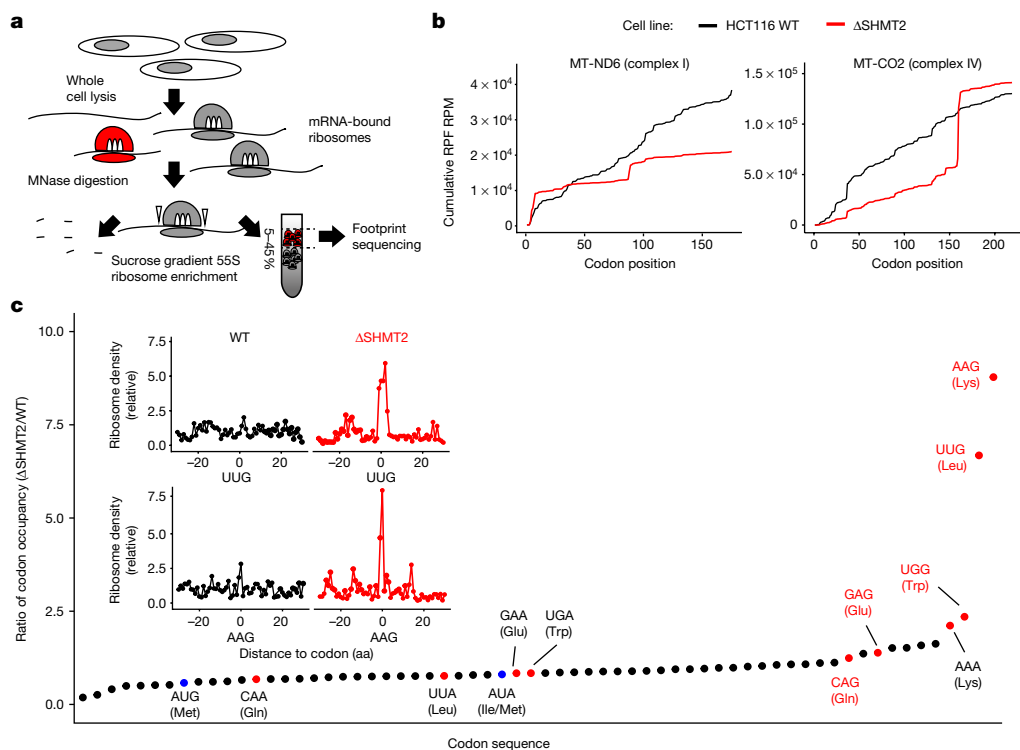


Figure 3 | Mitochondrial ribosome profiling reveals that SHMT2-knockout cells are deficient in translating specific guanosine-ending codons. **a**, Workflow of mitochondrial ribosome profiling. Translation was halted using chloramphenicol and immersion into liquid nitrogen, cells were lysed and RNA was digested using micrococcal nuclease (MNase). After sucrose-gradient enrichment for mitochondrial ribosomes (shaded in red), protected fragments were sequenced. **b**, Mean cumulative ribosome density along selected mitochondrial transcripts. Additional transcripts are given in Extended Data Fig. 6a. RPF, ribosome-protected

fragment; RPM, reads per million. **c**, Mean codon-specific mitochondrial ribosome occupancy in HCT116 cells (Δ SHMT2/wild type). Red data points correspond to codons that are decoded by tRNAs carrying the 5-taurinomethyluridine (τ m⁵U) modification. Red labels correspond to the subset of codons that end in guanosine and thus require wobble-base pairing. Methionine codons are highlighted in blue and show no increased codon occupancy. The insert shows mean normalized ribosome density relative to UUG and AAG codon position. aa, amino acids. Data in **b** and **c** represent two technical replicates of two independent samples.

This did not seem to reflect a shortage of these amino acids or tRNAs in mitochondria, as much less stalling was observed at the corresponding Lys^{AAA} and Leu^{UUA} codons. Instead, it appeared to relate to difficulty in reading the 3' codon guanosine of certain codons: those in which the 3' position identity (purine versus pyrimidine) determines the encoded amino acid ('split codon boxes'; Extended Data Fig. 6d). Increased codon occupancy was observed also for Trp^{UGG}, Glu^{GAG} and Gln^{CAG}, but not the corresponding codons with 3' adenosine. The sole exception was Met^{AUG/AUA}, in which no stalling was observed. Decoding of A/G-ending codons in split codon boxes is facilitated by methyl-derivative base modifications of the tRNA anticodon 5' nucleotide, allowing non-Watson-Crick base-pairing with the codon 3' base²² (Fig. 4a). The mitochondrial tRNA^{Met} anticodon has a 5' cytidine that is formylated with the 1C unit derived from S-adenosyl-methionine (SAM)²³. By contrast, the mitochondrial tRNAs for Lys, Leu1 (one of two mitochondrial leucine tRNAs), Trp, Glu and Gln have uridine at the 5' anticodon position²⁴. Mammalian cytosolic tRNAs with uridine at the anticodon 5' position are modified to produce 5-methoxycarbonylmethyluridine (mcm⁵U), with the methoxy carbon derived from SAM^{25,26}. Corresponding mitochondrial tRNAs are 5-taurinomethyl modified at the 5' anticodon uridine (τ m⁵U at position 34 of the tRNA)^{27–29}. As SHMT2/MTHFD2 double-knockout cell lines supplemented with sarcosine showed rescue of codon-specific stalling on mitochondrial ribosome profiling (Extended Data Fig. 6e), we hypothesized that the τ m⁵U modification is dependent on mitochondrial methylene-THF and that the observed oxidative phosphorylation defect is a consequence of impaired translation due to defective tRNA modification.

To test this hypothesis, we established a liquid chromatography-mass spectrometry (LC-MS) method for detection of modified

mitochondrial tRNA bases. In SHMT2-knockout cell lines, levels of formylcytidine were unchanged (Extended Data Fig. 7a). By contrast, τ m⁵U and its 2-thio derivative (in which the uracil 2-position oxygen is replaced with sulfur) were depleted to undetectable levels (Fig. 4b and Extended Data Fig. 7b). The depletion was not due to a lack of taurine, the cellular levels of which tended to be higher (Extended Data Fig. 7c). The loss of τ m⁵U and its 2-thio derivative was reversed upon re-expression of wild-type SHMT2 and also upon sarcosine supplementation of SHMT2/MTHFD2 double-knockout cells (Extended Data Fig. 7d, e). Thus, SHMT2 or an alternative source of mitochondrial methylene-THF is required to produce τ m⁵U.

To verify that the methyl group of τ m⁵U is coming from methylene-THF made by SHMT2, we conducted stable isotope tracing with ¹³C-labelled serine (the SHMT2 substrate) versus [¹³C]methionine (which feeds into SAM). As expected, methionine labelled formylcytidine. By contrast, serine labelled τ m⁵U, but methionine did not (Extended Data Fig. 7f). Thus, SHMT2 is required for oxidative phosphorylation because it produces mitochondrial methylene-THF for tRNA taurinomethylation. To our knowledge, this is the first direct evidence of folate-dependent macromolecule modification in mammalian cells.

The enzyme complex that catalyses the τ m⁵U base modification in mitochondria comprises two proteins, MTO1 and GTPBP3, both of which are encoded by genes that are mutated in human mitochondrial diseases^{30,31}. Orthologues of the enzyme complex, forming the prokaryotic tRNA-modifying MnmE/GidA complex, have been shown to use THF-bound 1C units³². We therefore explored whether the mitochondrial translation defect upon SHMT2 loss matches human diseases proposed to affect taurinomethylation of mitochondrial tRNAs^{27,28,30,31}. Indeed, MTO1 knockout in HCT116 cells caused loss

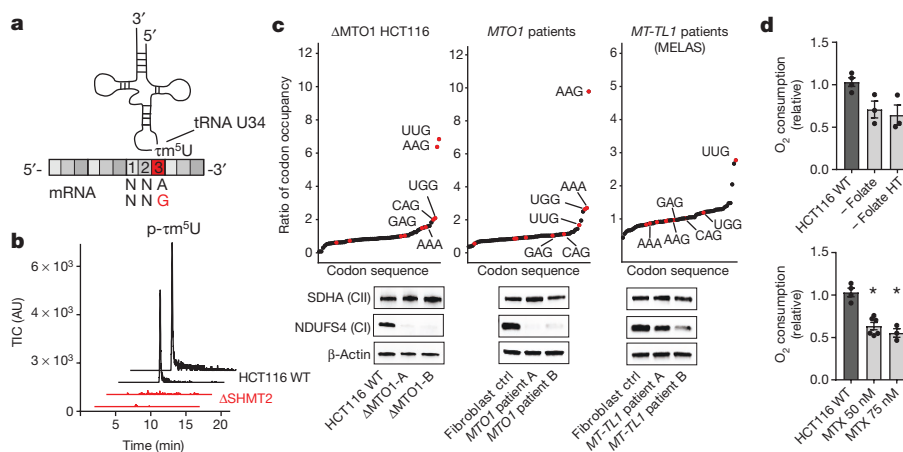


Figure 4 | MTO1/GTPBP3-dependent tRNA methylation requires mitochondrial methylene-THF. **a**, Interaction of tRNA position 34 anticodon loop modified base with mRNA codon 3 position A/G, forming a non-Watson–Crick base pair. **b**, Total ion chromatogram of 5-taurinomethyluridine monophosphate (p-tm⁵U) ($m/z = 460.043$) from digested mitochondrial tRNAs. 5-formylcytidine monophosphate was not altered (Extended Data Fig. 7a). **c**, Mean codon-specific mitochondrial ribosome occupancy for MTO1-knockout (ΔMTO1) HCT116 cell lines and primary patient-derived fibroblasts carrying MTO1 mutations

of tm⁵U (Extended Data Fig. 7e). Mitochondrial ribosome profiling of these engineered MTO1-deletion cells showed an increase in codon occupancy at the same codons as with SHMT2 knockout (Fig. 4c). In both cases, the strongest stalling occurred at Lys^{AAG} and Leu^{UUG}, potentially because these codons have, in addition to the wobble base pairing, only A–U base pairings versus the stronger C–G base pairings in Glu^{GAG}, Gln^{CUG} and Trp^{UGG} codons³³. Mitochondrial ribosome profiling of primary fibroblasts of two patients carrying different MTO1 missense mutations revealed increased codon occupancy selectively at Lys^{AAG}, but not Leu^{UUG}. Thus, these hypomorphic mutations seem to cause a selective defect in taurinomethylation of the Lys tRNA. Of all adenosine-ending codons, Lys^{AAA} showed the greatest increase in codon occupancy across all cell lines, being most pronounced in the MTO1 patients (Fig. 4c).

Notably, in both SHMT2 and MTO1 deletion cells, stalling did not affect all AAG and UUG codons uniformly, but occurred most strongly at the same specific gene locations (Extended Data Fig. 7g). Mapping of AAG and UUG codons at stalling sites relative to mRNA secondary structure³⁴ did not reveal any clear pattern (Extended Data Fig. 8a, b and Supplementary Tables 4, 5). Mapping onto the structure of the protein being synthesized (Extended Data Fig. 8c), however, showed a trend towards stalling at transitions between transmembrane helices and non-membrane domains (Supplementary Table 5). Thus, stalling due to the defective codon–anticodon interaction might be exacerbated by particular protein sequence features.

Defined mutations in the Lys and Leu1 mitochondrial tRNAs (which decode the most strongly affected Lys^{AAG} and Leu^{UUG} codons) result in a tRNA-specific tm⁵U modification defect, causing the human mitochondrial disorders MERRF and MELAS^{27,28}. Mitochondrial ribosome profiling of fibroblasts from two patients with MELAS due to the m.3243A>G mutation in the *MT-TL1* gene revealed, as expected³⁵, increased occupancy at Leu^{UUG} but not Lys^{AAG} or Leu^{UUA} (Fig. 4d). For unknown reasons, increased ribosome occupancy for either Ser^{AGU} or Thr^{ACG} was also observed in individual patients (Extended Data Fig. 9a). The extent of stalling and complex I depletion was less than with nuclear *SHMT2* or *MTO1* mutations, presumably owing to the heteroplasmic nature of the mitochondrial tRNA mutation (Fig. 4c and Extended Data Fig. 9b). Collectively these observations highlight a common biochemical mechanism that links mitochondrial folate metabolism with a considerable fraction of inborn errors of mitochondrial metabolism^{27,28,30,31}.

or the *MT-TL1* m.3243A>G MELAS variant ($n = 2$). Corresponding immunoblots are shown below. Individual patient data are in Extended Data Fig. 9a. **d**, Basal respiration rates measured using the Seahorse XF analyser. Data were collected after growth in the absence (–) of folate for 5 passages or in the presence of the indicated methotrexate (MTX) concentration for 96 h ($n = 3$, except HCT116 WT $n = 4$ and MTX 50 nM $n = 6$). HT, 100 μM hypoxanthine and 16 μM thymidine. Data are mean ± s.e.m. n indicates the number of biological replicates. * $P < 0.01$, two-tailed Student's t -test (see Supplementary Table 7 for exact P values).

On the basis of these observations, we wondered whether folate deficiency, which in pregnancy causes neural tube defects^{1–3}, could also result in mitochondrial impairment. Consistent with such a possibility, growth of HCT116 wild-type cells in folate-deficient media resulted in decreased levels of complex I enzymes and a reduced basal respiration rate (Fig. 4d and Extended Data Fig. 10a), without affecting mitochondrial DNA content (Extended Data Fig. 10b). In individuals with adequate nutrition, functional folate deficiency can be caused by antifolate therapy for autoimmunity or cancer. Low doses of the antifolate methotrexate, resulting in up to 100 nM circulating drug concentrations, are commonly used to treat autoimmune diseases such as rheumatoid arthritis^{4,36}. In cell culture, nanomolar concentrations of methotrexate resulted in decreased levels of complex I enzymes and oxygen consumption (Fig. 4d and Extended Data Fig. 10c). Thus, the essential role for folate metabolism in mitochondrial translation may contribute to the clinical manifestations of folate deficiency and the clinical efficacy of antifolate therapies.

Online Content Methods, along with any additional Extended Data display items and Source Data, are available in the online version of the paper; references unique to these sections appear only in the online paper.

Received 7 June; accepted 14 December 2017.

Published online 24 January 2018.

1. Fox, J. T. & Stover, P. J. Folate-mediated one-carbon metabolism. *Vitam. Horm.* **79**, 1–44 (2008).
2. Tibbetts, A. S. & Appling, D. R. Compartmentalization of mammalian folate-mediated one-carbon metabolism. *Annu. Rev. Nutr.* **30**, 57–81 (2010).
3. Ducker, G. S. & Rabinowitz, J. D. One-carbon metabolism in health and disease. *Cell Metab.* **25**, 27–42 (2017).
4. Lipsky, P. E. *et al.* Infliximab and methotrexate in the treatment of rheumatoid arthritis. *N. Engl. J. Med.* **343**, 1594–1602 (2000).
5. Chabner, B. A. & Roberts, T. G. Jr. Timeline: chemotherapy and the war on cancer. *Nat. Rev. Cancer* **5**, 65–72 (2005).
6. Ron-Harel, N. *et al.* Mitochondrial biogenesis and proteome remodeling promote one-carbon metabolism for T cell activation. *Cell Metab.* **24**, 104–117 (2016).
7. Nilsson, R. *et al.* Metabolic enzyme expression highlights a key role for MTHFD2 and the mitochondrial folate pathway in cancer. *Nat. Commun.* **5**, 3128 (2014).
8. Kim, D. *et al.* SHMT2 drives glioma cell survival in ischaemia but imposes a dependence on glycine clearance. *Nature* **520**, 363–367 (2015).
9. Ducker, G. S. *et al.* Reversal of cytosolic one-carbon flux compensates for loss of the mitochondrial folate pathway. *Cell Metab.* **23**, 1140–1153 (2016).
10. Garrow, T. A. *et al.* Cloning of human cDNAs encoding mitochondrial and cytosolic serine hydroxymethyltransferases and chromosomal localization. *J. Biol. Chem.* **268**, 11910–11916 (1993).

11. Gohil, V. M. *et al.* Nutrient-sensitized screening for drugs that shift energy metabolism from mitochondrial respiration to glycolysis. *Nat. Biotechnol.* **28**, 249–255 (2010).
12. Mullen, A. R. *et al.* Reductive carboxylation supports growth in tumour cells with defective mitochondria. *Nature* **481**, 385–388 (2011).
13. Sullivan, L. B. *et al.* Supporting aspartate biosynthesis is an essential function of respiration in proliferating cells. *Cell* **162**, 552–563 (2015).
14. Birsoy, K. *et al.* An essential role of the mitochondrial electron transport chain in cell proliferation is to enable aspartate synthesis. *Cell* **162**, 540–551 (2015).
15. Iborra, F. J., Kimura, H. & Cook, P. R. The functional organization of mitochondrial genomes in human cells. *BMC Biol.* **2**, 9 (2004).
16. Brown, S. S., Neal, G. E. & Williams, D. C. Subcellular distribution of some folic acid-linked enzymes in rat liver. *Biochem. J.* **97**, 34C–36C (1965).
17. Anderson, D. D., Quintero, C. M. & Stover, P. J. Identification of a de novo thymidylate biosynthesis pathway in mammalian mitochondria. *Proc. Natl Acad. Sci. USA* **108**, 15163–15168 (2011).
18. Kozak, M. Comparison of initiation of protein synthesis in procaryotes, eucaryotes, and organelles. *Microbiol. Rev.* **47**, 1–45 (1983).
19. Tucker, E. J. *et al.* Mutations in MTFMT underlie a human disorder of formylation causing impaired mitochondrial translation. *Cell Metab.* **14**, 428–434 (2011).
20. Saada, A. *et al.* Mutant mitochondrial thymidine kinase in mitochondrial DNA depletion myopathy. *Nat. Genet.* **29**, 342–344 (2001).
21. Calvo, S. E. & Mootha, V. K. The mitochondrial proteome and human disease. *Annu. Rev. Genomics Hum. Genet.* **11**, 25–44 (2010).
22. Agris, P. F., Vendeix, F. A. & Graham, W. D. tRNA's wobble decoding of the genome: 40 years of modification. *J. Mol. Biol.* **366**, 1–13 (2007).
23. Van Haute, L. *et al.* Deficient methylation and formylation of mt-tRNA^{Met} wobble cytosine in a patient carrying mutations in NSUN3. *Nat. Commun.* **7**, 12039 (2016).
24. Pütz, J., Dupuis, B., Sissler, M. & Florentz, C. Mamit-tRNA, a database of mammalian mitochondrial tRNA primary and secondary structures. *RNA* **13**, 1184–1190 (2007).
25. Fu, Y. *et al.* The AlkB domain of mammalian ABH8 catalyzes hydroxylation of 5-methoxycarbonylmethyluridine at the wobble position of tRNA. *Angew. Chem. Int. Ed. Engl.* **49**, 8885–8888 (2010).
26. Songe-Møller, L. *et al.* Mammalian ALKBH8 possesses tRNA methyltransferase activity required for the biogenesis of multiple wobble uridine modifications implicated in translational decoding. *Mol. Cell. Biol.* **30**, 1814–1827 (2010).
27. Yasukawa, T. *et al.* Defect in modification at the anticodon wobble nucleotide of mitochondrial tRNA^{lys} with the MERRF encephalomyopathy pathogenic mutation. *FEBS Lett.* **467**, 175–178 (2000).
28. Yasukawa, T., Suzuki, T., Ueda, T., Ohta, S. & Watanabe, K. Modification defect at anticodon wobble nucleotide of mitochondrial tRNAs^{Leu}(UUR) with pathogenic mutations of mitochondrial myopathy, encephalopathy, lactic acidosis, and stroke-like episodes. *J. Biol. Chem.* **275**, 4251–4257 (2000).
29. Suzuki, T. & Suzuki, T. A complete landscape of post-transcriptional modifications in mammalian mitochondrial tRNAs. *Nucleic Acids Res.* **42**, 7346–7357 (2014).
30. Ghezzi, D. *et al.* Mutations of the mitochondrial-tRNA modifier *MTO1* cause hypertrophic cardiomyopathy and lactic acidosis. *Am. J. Hum. Genet.* **90**, 1079–1087 (2012).
31. Kopajtich, R. *et al.* Mutations in *GTPBP3* cause a mitochondrial translation defect associated with hypertrophic cardiomyopathy, lactic acidosis, and encephalopathy. *Am. J. Hum. Genet.* **95**, 708–720 (2014).
32. Moukadir, I. *et al.* Evolutionarily conserved proteins MnmE and GidA catalyze the formation of two methyluridine derivatives at tRNA wobble positions. *Nucleic Acids Res.* **37**, 7177–7193 (2009).
33. Doherty, E. A., Batey, R. T., Masquida, B. & Doudna, J. A. A universal mode of helix packing in RNA. *Nat. Struct. Biol.* **8**, 339–343 (2001).
34. Rouskin, S., Zubradt, M., Washietl, S., Kellis, M. & Weissman, J. S. Genome-wide probing of RNA structure reveals active unfolding of mRNA structures *in vivo*. *Nature* **505**, 701–705 (2014).
35. Kirino, Y., Goto, Y., Campos, Y., Arenas, J. & Suzuki, T. Specific correlation between the wobble modification deficiency in mutant tRNAs and the clinical features of a human mitochondrial disease. *Proc. Natl Acad. Sci. USA* **102**, 7127–7132 (2005).
36. Grim, J., Chládek, J. & Martínková, J. Pharmacokinetics and pharmacodynamics of methotrexate in non-neoplastic diseases. *Clin. Pharmacokinet.* **42**, 139–151 (2003).
37. Mayr, J. A. *et al.* Spectrum of combined respiratory chain defects. *J. Inher. Metab. Dis.* **38**, 629–640 (2015).

Supplementary Information is available in the online version of the paper.

Acknowledgements We thank T. Pan, W. Lu, L. Chen, L. Parsons, W. Wang and T. Srikanth, and all members of the Rabinowitz laboratory. This work was supported by funding to J.D.R. from the US National Institutes of Health (NIH) (R01CA163591 and DP1DK113643) and StandUp to Cancer (SU2C-AACR-DT-20-16). G.S.D. was supported by a postdoctoral fellowship (PF-15-190-01-TBE) from the American Cancer Society. J.A.M. was supported by the science fund of the Paracelsus Medical University Salzburg (E-12/15/076-MAY). Z.G. was supported by the NIH (DP1AI124669).

Author Contributions R.J.M., G.S.D. and J.D.R. conceived the project and designed the experiments. R.J.M. and J.D.R. wrote the manuscript. R.J.M., G.S.D. and S.H.L. performed biochemical experiments. Z.G. and W.S. were involved in study design and data interpretation. W.S. and J.A.M. contributed primary patient cell lines. All authors reviewed and edited the manuscript before submission.

Author Information Reprints and permissions information is available at www.nature.com/reprints. The authors declare competing financial interests: details are available in the online version of the paper. Readers are welcome to comment on the online version of the paper. Publisher's note: Springer Nature remains neutral with regard to jurisdictional claims in published maps and institutional affiliations. Correspondence and requests for materials should be addressed to J.D.R. (joshr@princeton.edu).

Reviewer Information *Nature* thanks D. Appling, V. Gohil and the other anonymous reviewer(s) for their contribution to the peer review of this work.

METHODS

Cell lines and growth conditions. HCT116 (CCL-247) and HEK293T/17 (CRL-11268) were purchased from ATCC. Generation of a subset of clonal CRISPR-Cas9 knockout cell lines and detailed characterization has been reported previously⁹. Additional clonal knockout cell lines (Supplementary Table 6a) were established following the protocol published previously³⁸. In brief, exon-targeting guide RNAs (Supplementary Table 6b) were designed against genes of interest and cloned into an expression vector containing the double nicking Cas9 variant (Addgene). Cells were transiently transfected using Lipofectamine 2000 (Life Technologies) (HEK293T) or Fugene HD (Promega) (HCT-116) and selected for 48 h with 2 µg ml⁻¹ puromycin. Single clones were isolated using serial dilution into 96-well plates.

Stable SHMT2 re-expression was achieved by transfecting HEK293T knockout cell lines with NM_005412.5 cDNA (GE Healthcare) cloned into pCMV-Tag8 vector (Agilent) and selection for three weeks with 200 µg ml⁻¹ hygromycin B (Sigma-Aldrich). Catalytic inactive (p.Glu98Leu/p.Tyr106Phe)^{39,40} and PLP-binding deficient (p.Lys280Gln)⁴¹ mutants were obtained following the QuickChange II protocol (Agilent). Knockout and re-expression cell lines were functionally verified by immunoblotting followed by targeted genomic sequencing (Supplementary Fig. 9) and, in the case of SHMT2 cell lines, also by tracing of [2,3,3-²H]serine labelling into dTTP. *MTO1* and *MT-TL1* patient fibroblasts and controls were provided by the Department of Paediatrics, Salzburg Landeskliniken and Paracelsus Medical University, Salzburg. Studies with primary human cell lines were approved by the local ethics-committee and informed consent was obtained from all subjects. The genotypes of *MTO1*-deficient patients (GenBank NM_012123.3) were as follows: patient-A c.[1261-5T>G];[1430G>A], (p.[?];[Arg477His]); patient-B c.[1222T>A];[1222T>A], (p.[Ile408Phe];[Ile408Phe]). Patient-B *MTO1* has been reported before⁴². Both MELAS patients carried the common *MT-TL1* m.3243A>G mutation with the heteroplasmy rate reported in this study (Extended Data Fig. 9b). All cell lines tested negative for mycoplasma and were cultured in DMEM without sodium pyruvate (Sigma-Aldrich) supplemented with 10% dialysed fetal bovine serum (dFBS, GE Healthcare) in a 5% CO₂ incubator at 37 °C. No antibiotics were used.

Glucose uptake and lactate secretion. Cells were seeded in 6-well plates 24 h before the start of an experiment. After reaching 50% confluency, plates were washed with PBS (GE Healthcare) and 3 ml of fresh media was added. Glucose uptake and lactate secretion were determined using a YSI 2900D Biochemistry Analyzer (Xylem Analytics) and normalized to cell growth as determined by micro-litre packed cell volume (PCV; as measured using packed cell volume microfuge tubes from TPP).

Proliferation. Proliferation assays were conducted in 96-well plates and relative cell number was measured using resazurin sodium salt. Approximately 5,000 cells were plated in each well with 150 µl DMEM supplemented with 10% dFBS. Cell growth at each day was read as fluorescence intensity using a Synergy HT plate reader (BioTek Instruments).

Oxygen consumption. Oxygen consumption rates were measured on a XF24 extracellular flux analyser (Agilent) following the manufacturer's instructions. In brief, XF24 cell culture microplates were coated with fibronectin (Sigma-Aldrich) and cells were seeded at 5 × 10⁴ (HEK293T) and 7 × 10⁴ (HCT116) cells per well. After reaching 70–90% confluency, cells were equilibrated for 1 h in XF assay medium supplemented with 10 mM glucose, 1 mM sodium pyruvate, and 2 mM glutamine in a non-CO₂ incubator. Oxygen consumption rates were monitored at baseline and throughout sequential injections of oligomycin (1 µM), carbonyl cyanide-4-(trifluoromethoxy)phenylhydrazone (1 µM) and rotenone/antimycin A (0.5 µM each). Data for each well were normalized to cell number as determined by CyQUANT Cell Proliferation Assay Kit (Invitrogen) and to the on-plate wild-type control. For absolute oxygen consumption rate values, the protein concentration was determined by BCA protein assay (Thermo Fisher Scientific).

Immunoblotting. Cells were cultured to sub-confluency in 6 cm plates. After removal of media, cells were rinsed with 4 °C PBS and lysed in radio-immunoprecipitation assay (RIPA) buffer with phosphatase and protease inhibitors (Roche). Lysates were cleared by 10 min centrifugation at 16,000 g and quantified using a BCA assay (Pierce). Samples were resolved by SDS-PAGE on precast gels (Bio-Rad) and transferred to a nitrocellulose membrane using the Trans-Blot Turbo system (Bio-Rad). After overnight incubation with primary antibodies, bands were visualized with horseradish peroxidase-conjugated secondary antibodies (Cell Signaling Technologies). ChemiDoc XRS+ system was used for image acquisition. The following antibodies were used according to their manufacturer's directions: anti-SHMT1 (12612), anti-SHMT2 (12762), anti-MRPL11 (2066), anti-S6RP (2217) and anti-β-actin (5125) were from Cell Signaling Technologies; anti-MTHFD2 (ab151447), anti-NDUFS4 (ab139178), anti-SDHA (ab14715) and anti-VDAC (ab14734) were from Abcam; anti-MTHFD1L (HPA029041) was from Sigma-Aldrich.

Analysis of mitochondrial specific translation. ³⁵S-labelling of mitochondrial proteins was performed following the method described previously⁴³. In brief, cells were grown on 6 cm plates for 48 h to sub-confluency. Then media was changed to DMEM with 10% dFBS without methionine (MP Biomedicals). After a 30 min incubation, cytosolic translation was inhibited by emetine hydrochloride (0.1 mg ml⁻¹, Sigma-Aldrich) and labelling was conducted for 1 h after the addition of 500 µCi [³⁵S]methionine (EasyTag L [³⁵S]-Methionine, Perkin Elmer). Protein lysates (30 µg) were then separated on a 15% polyacrylamide gel (8.3 × 7.3 cm) and dried using a 443 Slab Dryer (BioRad). The dried gel was exposed to a storage phosphor screen (GE Healthcare) and imaged on a Typhoon FLA 9500 (GE Healthcare). Equal sample loading was confirmed by Coomassie brilliant blue staining (BioRad).

Metabolite concentrations and labelling patterns. Cells were grown in 6-cm dishes for at least 48 h and collected at 75% confluency. Media was replaced every 24 h and additionally 6 h before collection. Metabolism was quenched and metabolites were extracted by aspirating media and immediately adding 1 ml of 80:20 methanol:water at -80 °C. Plates were kept on ice, scraped and non-soluble debris was pelleted at 18,000 g for 10 min. Samples were directly analysed by hydrophilic interaction chromatography coupled with negative-mode electrospray-ionization high resolution mass spectrometry on a quadrupole-orbitrap scanning from *m/z* 73 to 1,000 at 1 Hz and 140,000 resolution (Q Exactive Plus, Thermo-Fisher). Liquid chromatography separation was achieved on a XBridge BEH Amide column (2.1 mm × 150 mm, 2.5 µm particle size, 130 Å pore size; Waters) using a gradient of solvent A (20 mM ammonium acetate + 20 mM ammonium hydroxide in 95:5 water:acetonitrile, pH 9.45) and solvent B (acetonitrile). Flow rate was 150 µl min⁻¹. The gradient was: 0 min, 85% B; 2 min, 85% B; 3 min, 60% B; 9 min, 60% B; 9.5 min, 35% B; 12 min, 35% B; 12.5 min, 0% B; 18 min, 0% B; 18.5 min, 85% B; 23 min, 85% B. Data were processed and analysed using MAVEN software⁴⁴. All isotope tracer experiments were conducted at isotopic steady state: [2,3,3-²H]serine was traced into dTTP for a minimum of 6 h and [3-¹³C]serine and [U-¹³C]methionine were traced into tRNA for a minimum of 4 days. Isotopic tracers were purchased from Cambridge Isotope Laboratories. Isotopically labelled media was prepared from scratch and supplemented with 10% dFBS.

RNA sequencing. RNA was isolated from cell lines using RNeasy Plus kit (Qiagen) according to the manufacturers' recommendation. After the depletion of ribosomal RNA, libraries were prepared according to the TruSeq Stranded Total RNA protocol (Illumina) and sequencing was performed on a HiSeq 2500 (Illumina). Analysis was performed using the Galaxy system⁴⁵ and the R software package⁴⁶. Adaptor sequences were trimmed using Cutadapt (Galaxy version 1.6)⁴⁷ and the trimmed reads were then mapped with TopHat (Galaxy Version 0.9)⁴⁸ to the GRCh38 reference using ENSEMBL version 80 genes as known splice junctions. The read counts per gene were determined using htseq-count (Galaxy Version 0.6.1galaxy1)⁴⁹ in 'union' mode. Differential expression analysis was performed in R using DESeq2 1.12.3 package⁵⁰. SHMT2-knockout gene expression (log₂ RPKM) was graphed relative to the wild-type and the re-expressed cell lines.

Mitochondrial DNA content and integrity. To analyse mitochondrial DNA content, total DNA was extracted from 7 × 10⁶ cells using Gentra Puregene Cell Kit (Qiagen) after freezing the cell pellet at -80 °C for 1 h and overnight digestion with Proteinase K (Roche Diagnostics). qPCR (ViiA 7, Applied Biosystems) was performed using primers targeting the mitochondrial *ND2* locus (also known as *MT-ND2* pseudogene 1) (forward: 5'-TGTTGGTTATACCCCTCCCGTACTA-3'; reverse: 5'-CCTGC AAAGATGGTAGAGTAGATGA-3') and a nuclear *ALU* repeat sequence (forward: 5'-CTTGCAGTGAGCCGAGATT-3'; reverse: 5'-GAGACGGA GTCTCGCTCTGTC-3') as published earlier⁵¹. The relative mitochondrial DNA content was determined using the ΔΔC_t method. Each independent sample given in the figures represents the mean of 6 technical replicates.

The mitochondrial genome was screened for deletions by long range PCR with two primer pairs spanning the whole coding region (forward_1: CCAACCAAACCCCAAAGAC, reverse_1: TACTGCGACATAGGGTGCTC; forward_2: CACCAGCCTAACCAGATTTC reverse_2: tggaccacaaatctgctcc) and products run on a 1% agarose gel⁵². DNA from a mitochondrial DNA deletion patient was used as positive control.

For mitochondrial genomic sequence analysis, mtDNA was enriched using the multiple displacement amplification strategy (REPLI-g, Qiagen) and sequencing was performed on a HiSeq 2500 after library preparation following the Nextera library prep kit protocol (Illumina). Reads were mapped to GRCh38 using Bowtie2 (Galaxy Version 0.6)⁵³ with default settings. Coverage plots were generated using DeepTools bamCoverage (Galaxy Version 2.3.6.0)⁵⁴. The data were normalized to 1 × coverage using an effective genome size of 16,569. Freebayes (Galaxy Version 0.4.1)⁵⁵ with frequency-based pooled settings was used to generate the variant data. The figures were generated in R using Gviz 1.18.0⁵⁶.

The *MT-TL1* mutation load was determined using primers specifically spanning the m.3243 position for targeted enrichment (forward: 5'-AATGATACGGCGAC CACCGAGATCTACACNNNNNGCCTTCCCCGTAATGATA-3', reverse: 5'-CAAGCAGAAGACGGCATAACGAGATCGTCAGCGAAGGGTTGTAGT-3') followed by sequencing on a MiSeq nano flow cell using a custom sequencing primer (sequence: TATTATACCCACCCACCCAAGAAGGGTTGTAAAG). Alignment to GRCh38 was performed using Bowtie2 (Galaxy Version 0.6)⁵³ at default settings and position-specific mutation load was derived from the Integrative Genomics Viewer.

Mitochondrial ribosome profiling. Development of our ribosome profiling method was based on concepts reported previously^{57–59}. For mitochondrial ribosome profiling, cell lines were grown on 15-cm plates to 70–85% confluency. Sarcosine rescue of ribosome stalling in the SHMT2/MTDF2 double-knockout background was assessed after growth in the presence of 1 mM sarcosine for 5 days. After removal of media, plates were rapidly rinsed with ice-cold PBS containing chloramphenicol (100 µg ml⁻¹) (Sigma-Aldrich) and cycloheximide (100 µg ml⁻¹) (Sigma-Aldrich) followed by immediate immersion into liquid nitrogen. Plates were then transferred to wet ice and 1 ml of 1.5× lysis buffer was added and the lysate was collected using a cell scraper. Lysis buffer contained the following: 1.5% Triton X-100 (Sigma-Aldrich), 0.15% NP40 (Sigma-Aldrich), 1× complete phosphatase and protease inhibitors (Roche), and 30 U ml⁻¹ DNase 1 (Roche) in buffer base (20 mM Tris-HCl pH 7.8 (Ambion), 100 mM KCl (Ambion), 10 mM MgCl₂ (Ambion), 100 µg ml⁻¹ chloramphenicol, 100 µg ml⁻¹ cycloheximide). 1.6–1.8 ml were recovered per plate and homogenized by passing three times through a 32G needle at 4°C. Non-soluble debris was pelleted at 5,000 g for 10 min and 1,520 µl supernatant was used for digestion with 7,500 U ml⁻¹ micrococcal nuclease (Roche) after adding 40 µl SUPERaseIN (Ambion) and 5 mM CaCl₂ (Ambion). Digestion was stopped after 1 h gentle shaking at 25°C using a final concentration of 6 mM EGTA.

Buffer base was used to make 5%–45% sucrose gradients (Gradient Master, Biocomp). After cooling to 4°C, samples were separated in an ultracentrifuge using the SW-41Ti rotor at 210,000g for 2.5 h. Live UV absorption at 254 nm was used to track the mitochondrial 55S monosome enriched fractions (Extended Data Fig. 5b). The 55S fractions were pooled and mixed with 57 µl 20% SDS per millilitre sample before performing acid phenol chloroform RNA extraction. RNA was precipitated using 300 mM sodium acetate pH 5.5 and equal volume isopropanol and run on a 15% TBE-urea gel (Invitrogen) at 210 V for 1 h for size selection. Gels were stained with Sybr Gold (Invitrogen) and RNA fragments corresponding to mitochondrial ribosome footprints (approximately 28–40 nucleotides) were cut and recovered from the gel using the crush and soak method. After sodium acetate/isopropanol precipitation, library preparation was conducted following the TruSeq Ribo Profile (Illumina) protocol.

Sequencing of ribosome protected footprints (RPFs) was performed on a HiSeq 2500 in rapid mode followed by adaptor trimming using Cutadapt (Galaxy Version 1.6)⁴⁷. Reads were mapped to the human genome reference GRCh38 using BWA (Galaxy Version 0.9)⁴⁸ with those mapping to the mitochondrial protein-coding genes included in the subsequent analysis. The Plastid package⁶⁰ and customized Python and R⁴⁶ scripts were used for analysing mitochondrial ribosome profiling data. Alignment was performed from 3' of reads which was reported to yield superior results after digestion with Micrococcal nuclease^{61,62}. Each read, corresponding to a mitochondrial ribosome protected fragment (mtRPF), was assigned to a nucleotide position representing the respective ribosomal A-site as determined by metagenesis⁶⁰. mtRPF counts were then normalized to reads per million (RPM) mapped reads within each sample and single nucleotide positions were grouped by codon index. This transformation allows for relative quantification of bound ribosomes for each nucleotide triplet along a transcript. Stalling plots were created by plotting the mean cumulative mtRPF count along each mitochondrial open reading frame.

Codons were defined as stalling sites when the normalized counts mapped to the specific codon (mtRPF codon/mtRPF gene median) exceeded 2 s.d. from all codons in the genome. The relative abundance of actively translating ribosomes (that is, not stalled) was calculated by subtracting mtRPF counts in stalled regions from the total sum of ribosome footprints for each gene as $\Sigma \text{mtRPF}_{\text{active}} = \Sigma \text{mtRPF}_{\text{total}} - \Sigma \text{mtRPF}_{\text{stalled}}$. Then the gene specific ratio was plotted as $\Sigma \text{mtRPF}_{\text{active, SHMT2}} / \Sigma \text{mtRPF}_{\text{active, WT}}$. Stalling sites specific to the SHMT2-knockout condition were identified using the ratio of occupancy at each codon position relative to wild type. Specifically, codons were defined as SHMT2-specific stalling sites when the normalized counts in the mutant relative to wild type ($\Sigma \text{mtRPF}_{\text{codon, SHMT2}} / \Sigma \text{mtRPF}_{\text{codon, WT}}$) exceeded 2 s.d. (or, as indicated, 3 s.d.) from this ratio as determined for all codons in the genome, and the site also met the general stalling site criterion.

To determine the relative abundance of mitochondrial ribosomes bound to each nucleotide triplet, codon-specific occupancy ratios were calculated. For each codon (codon_{i=1–64}), the gene-specific ratio between experimentally measured

ribosome density and expected density (which is proportional to codon frequency) was calculated. Codon occupancy (CO_{i=1–64}) for each codon is the mean of the ratios from all 13 genes. The relative codon occupancy (CO_{i=1–64, SHMT2}) / (CO_{i=1–64, WT}) was plotted with error bars representing s.d. across replicates after error propagation. To investigate the ribosome distribution relative to the major stalled codons (AAG and UUG), ribosome densities flanking the codons of interest within 25 amino acids were selected. Each selected fragment was first normalized to its total count so every codon of interest from the genome is weighted equally. The mean value from each position was plotted.

Investigating protein secondary structure effects on stalling at AAG and UUG. On average stalling was most pronounced at AAG and UUG codons, but not all codons of the same sequence were equally affected. We therefore investigated whether the positioning relative to protein secondary structures (transmembrane helices) influences the extent of stalling. As micrococcal nuclease treatment induces imprecision in A-site mapping owing to sequence-biased digestion^{63,64}, individual positions identified as SHMT2-specific stalling sites were first grouped to the adjacent codons decoded by 5-taurinomethyluridine-modified tRNAs. Then amino acid residues corresponding to the AAG and UUG codons were mapped to *Bos taurus* crystal structures of mitochondrial respiratory chain complex proteins using iCn3D⁶⁵. Structure data was retrieved using the following Protein Data Bank (PDB) accession codes: ATP6: 5ARA_W; MT-CO2: 2Y69_B; MT-CYB: 1QCR_C; and MT-ND6: 5LDW_J (underscored suffixes denote the respective subunits of the supercomplexes). In addition, a hidden Markov model based algorithm for transmembrane helices (TMHMM 2.0⁶⁶) was used to predict α-helical transmembrane domains in the *Homo sapiens* sequences. This method assigns each codon a probability for transmembrane helix localization which was then used for genome wide assessment of AAG and UUG localization relative to transmembrane helices. AAG and UUG codons were defined to be at a transition between a transmembrane helix and a non-membrane region if, within the five flanking codons, probabilities >0.5 and <0.5 for being in a transmembrane helix are found. AAG and UUG codons were defined as stalling sites based on the 3 s.d. cut-off as per Extended Data Fig. 8b. In total, 4 out of 5 stalling AAG and UUG codons, and 7 out of 23 non-stalling AAG and UUG codons were at a membrane transition ($P=0.04$ by chi-square test).

Evaluation of mRNA secondary structure effects on ribosome stalling. To study a potential effect of mRNA secondary structure⁶⁷ (that is, base pairing) on ribosome stalling, we used the previously published dimethyl sulfate sequencing datasets on human K562 cell lines³⁴ to identify structured regions in mitochondrial transcripts. Following the methods described in the manuscript for nuclear transcripts, identification of sites with secondary structure was performed on mitochondrial transcript data³⁴. In brief, FASTQ files (accession numbers GSM1297495 and GSM1297493) were retrieved from sequence read archive and mapped to GRCh38 with BWA (Galaxy Version 0.9)⁴⁸. Reads were assigned to the nucleotide at the 5' end with no offset using Plastid⁶⁰. *R* values (cut-off 0.75) and Gini differences (cut-off 0.1) between the *in vivo* and denatured dataset were calculated for the complete mitochondrial transcriptome for a window size of 50 adenosine/cytosine nucleotides and a step size of 10. This provided a list of structured mitochondrial transcript regions, with most mRNA regions unstructured. The list of structured regions was compared to the SHMT2-specific stalling sites for potential co-localization. No stalling site mapped to a structured region.

Mitochondrial enzyme activities. Activities of individual OXPHOS complexes I–IV, ATP synthase and citrate synthase (which is nuclear encoded and was used as a marker of mitochondrial mass) were spectrophotometrically measured as previously described (Uvicon 922, Kontron)^{68–70}. Measurements were performed with 2 µl of mitochondria isolated by differential centrifugation⁷¹ (except for complex I, in which 10 µl was used).

Citrate synthase (EC 2.3.3.1) activity was determined following extinction dynamics at 412 nm, indicating the cleavage of Elman's reagent (0.2 mM) after addition of oxaloacetate (0.5 mM) to the buffered reaction solution containing acetyl-CoA (0.15 mM). Rotenone-sensitive complex I (NADH:decylubiquinone oxidoreductase, EC 1.6.5.3) activity was measured by adding NADH (0.2 mM) and monitoring at 340 nm for the reduction of decyl-ubiquinone (50 µM). Complex II (succinate:ubiquinone-oxidoreductase, EC 1.3.5.1) was measured at 600 nm by monitoring the reduction of 2,6-dichlorophenol-indophenol (80 µM) after addition of succinate (10 mM). The reaction mixture to determine complex III activity (coenzyme Q:cytochrome *c*-oxidoreductase, EC 1.10.2.2) contained cytochrome *c* (100 µM) and decyl-ubiquinol (200 µM) and was measured at 550 nm. After inhibition by addition of antimycin A (1 µM), the insensitive activity was subtracted to calculate specific complex III activity. The enzyme activity of complex IV (ferrocytochrome *c*:oxygen oxidoreductase, EC 1.9.3.1) was read as the oxidation rate of reduced cytochrome *C* (60 µM) at 550 nm. Complex V (F₁F₀ ATP synthase, EC 3.6.3.14) was indirectly measured as oligomycin-sensitive ATPase activity in a reaction mixture containing 0.5 mM ATP. Formed ADP was coupled

to a pyruvate kinase reaction, using phosphoenolpyruvate (2 mM) to generate ATP and pyruvate. The latter is then used by lactate dehydrogenase in the oxidation of NADH (0.2 mM) that served as readout (340 nm). Reagents were obtained from Sigma-Aldrich.

Mitochondrial tRNA modifications. HCT116 or HEK293T cell lines and clones were grown to 70–85% confluency and collected for mitochondrial extraction (1×10^8 – 2×10^8)⁷¹. Mitochondrial tRNAs were extracted using the MirVana miRNA Isolation kit (Ambion) for isolation of small RNAs followed by 10% TBE-urea gel purification and extraction as described above (tRNA fraction 65–85 base pairs). Quantitative analysis of 5-taurinomethyluridine monophosphate (p- τ m⁵U), 5-taurinomethyl-2-thiouridine monophosphate (p- τ m⁵s²U), 2-thiouridine monophosphate (p-s²U) and 5-formylcytidine monophosphate (p-f²C) was performed using high-resolution mass spectrometry following an adapted previously published protocol^{25,72}. In brief, 100 ng tRNA were digested at 37°C for 2 h by nuclease P1 (2 U) in 30 μ l of 100 mM ammonium acetate and quenched by adding 60 μ l 50/50 methanol/acetonitrile followed by centrifugation at 10,000 g for 10 min. 5 μ l of sample was injected for LC–MS analysis. Nucleoside monophosphates were analysed on a quadrupole-orbitrap mass spectrometer (Q Exactive plus, Thermo Fisher Scientific) operating in negative-ion mode coupled to hydrophilic interaction chromatography via electrospray ionization and used to scan in SIM mode from m/z 459 to 482 (τ m⁵U and τ m⁵s²U) or m/z 338 to 355 (s²U and f²C) at 1 Hz and 140,000 resolution. Consistent loading was ensured by measuring f²C levels (which are not altered by SHMT2 knockout) in the same sample as the τ m⁵U and τ m⁵s²U. The mass spectrometry standard for 5-taurinomethyluridine was synthesized as described previously⁷³ and was used to confirm peak identity in digested tRNA samples after an additional treatment with 1 U of alkaline phosphatase (Roche) in 100 mM ammonium carbonate at 37°C for 2 h⁷².

Folate depletion and methotrexate treatment. Cells were grown for five passages in folic acid-deficient DMEM with 10% dFBS (US Bio), either with or without hypoxanthine and thymidine supplementation (Gibco; final concentrations of 100 μ M sodium hypoxanthine and 16 μ M thymidine). To evaluate the effect of targeting IC-metabolism on mitochondrial function, methotrexate (Sigma-Aldrich) was used at 25, 50 and 75 nM concentration. Chloramphenicol (100 μ g ml⁻¹ = 310 μ M) and ethidium bromide (100 ng ml⁻¹ = 250 nM) served as positive controls for the inhibition of mitochondrial translation and mtDNA depletion respectively. At each time point, protein and DNA samples were collected for immunoblot and mtDNA content analysis. Basal respiration was assessed using the Seahorse XF analyser with measurements conducted as described above.

N-terminal protein formylation. N-formylmethionine modification on COX1 was assayed by mass spectrometry following the protocol described previously¹⁹. In brief, mitochondria were isolated from cells by differential centrifugation⁷¹ and complex IV was immunoprecipitated (ab109801, Abcam) before separation on a 4–20% polyacrylamide gel. A band running at the same molecular mass as a band reactive with an anti-COX1 antibody (ab14705, Abcam) was excised and lysed using 1.5 μ g LysC (Wako) as described⁷⁴. Samples were dried in a speedvac and re-suspended with 15 μ l of 0.1% formic acid pH 3. Per run, 5 μ l was injected using an Easy-nLC 1000 UPLC system. Samples were loaded directly onto a 45 cm \times 75 μ m nano-capillary column packed with 1.9 μ m C18-AQ (Dr. Maisch) mated to a metal emitter (Thermo Scientific) in-line with a Thermo Orbitrap Elite or Thermo Orbitrap Lumos. The mass spectrometer was operated in data-dependent mode with the 120,000 resolution MS1 scan (400–1,800 m/z) in the Orbitrap followed by up to 20 MS/MS scans in the ion trap. Raw files were searched using MS Amanda⁷⁵, Sequest HT⁷⁶ and Byonic⁷⁷ algorithms and validated using the Percolator algorithm⁷⁸ within the Proteome Discoverer 2.1 suite (Thermo Scientific). 10 p.p.m. MS1 and 0.6 Da MS2 mass tolerances were specified. Carbamidomethylation of cysteine was used as fixed modification and oxidation of methionine as dynamic modification. In addition, acetylation, formylation and loss of methionine were specified as potential modifications at the N terminus of proteins. The resulting msf file was used to construct a spectral library (percolator peptide $q > 0.95$) and extract MS1 ion chromatographs in Skyline^{79,80}. The fraction of modified N-terminal peptides of COX1 was calculated as the area of the formylated peptide divided by the sum of the areas of all the n-terminal peptides in that sample.

Statistics and reproducibility. Significance was determined by two-tailed Student's *t*-test comparing the indicated condition to the corresponding wild type or control. Asterisks denote $P < 0.01$. Exact *P* values for individual comparisons are given in Supplementary Table 7. Small filled circles are individual data points. All results have been independently replicated at least twice. This includes figure panels where representative data are shown. For quantitative measurements, *n* is provided in the figure legends. For western blots and DNA gels, we show representative data of multiple independent replicates: Fig. 1c ($n = 2$), Fig. 2b ($n = 3$), Fig. 4c ($n = 3$); Extended Data Fig. 1a ($n = 2$), Extended Data Fig. 1h ($n = 2$), Extended Data Fig. 1i ($n = 2$), Extended Data Fig. 2b ($n = 2$), Extended Data Fig. 2c ($n = 2$),

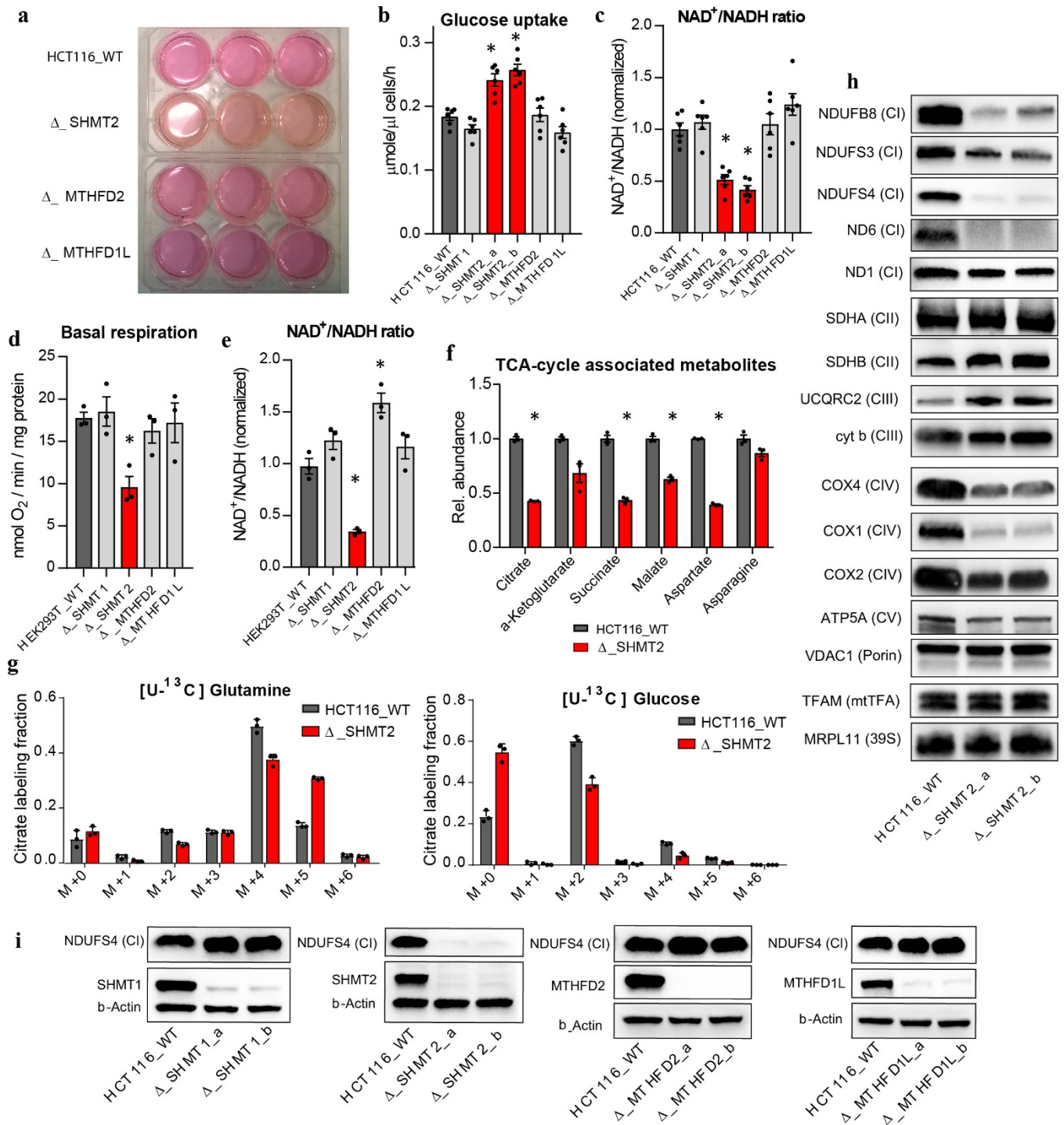
Extended Data Fig. 3a ($n = 2$), Extended Data Fig. 4d ($n = 2$), Extended Data Fig. 5a ($n = 2$), Extended Data Fig. 5b ($n = 3$), Extended Data Fig. 7f ($n = 2$), Extended Data Fig. 10a ($n = 3$) and Extended Data Fig. 10c ($n = 2$). No statistical methods were used to predetermine sample size. The experiments were not randomized, and investigators were not blinded to allocation during experiments and outcome assessment.

Code availability. All code used to generate the data in this manuscript is publicly available from GitHub (<https://github.com/R-J-Morscher>).

Data availability. Raw sequencing data are available from Sequence Read Archive (SRA) under BioProject accession number PRJNA419990. Source data for Figs 1c, 3c, 4c, Extended Data Figs 3d, 6e are provided with the paper. Uncropped versions of blots are provided in Supplementary Figs 1–8; Sanger sequencing traces are provided in Supplementary Fig. 9. Other data that support the findings of this study are available from the corresponding author upon request.

38. Ran, F. A. *et al.* Genome engineering using the CRISPR–Cas9 system. *Nat. Protocols* **8**, 2281–2308 (2013).
39. Szebenyi, D. M., Musayev, F. N., di Salvo, M. L., Safo, M. K. & Schirch, V. Serine hydroxymethyltransferase: role of glu75 and evidence that serine is cleaved by a retroaldol mechanism. *Biochemistry* **43**, 6865–6876 (2004).
40. Contestabile, R. *et al.* Role of tyrosine 65 in the mechanism of serine hydroxymethyltransferase. *Biochemistry* **39**, 7492–7500 (2000).
41. Iurescia, S., Condo, I., Angelaccio, S., Delle Fratte, S. & Bossa, F. Site-directed mutagenesis techniques in the study of *Escherichia coli* serine hydroxymethyltransferase. *Protein Expr. Purif.* **7**, 323–328 (1996).
42. Tischner, C. *et al.* MTO1 mediates tissue specificity of OXPHOS defects via tRNA modification and translation optimization, which can be bypassed by dietary intervention. *Hum. Mol. Genet.* **24**, 2247–2266 (2015).
43. Sasarman, F. & Shoubridge, E. A. Radioactive labeling of mitochondrial translation products in cultured cells. *Methods Mol. Biol.* **837**, 207–217 (2012).
44. Clasquin, M. F., Melamud, E. & Rabinowitz, J. D. LC–MS data processing with MAVEN: a metabolomic analysis and visualization engine. *Curr. Protoc. Bioinformatics* **Chapter 14**, Unit14.11 (2012).
45. Afgan, E. *et al.* The Galaxy platform for accessible, reproducible and collaborative biomedical analyses: 2016 update. *Nucleic Acids Res.* **44** (W1), W3–W10 (2016).
46. R Development Core Team. *R: A Language and Environment for Statistical Computing*; <http://www.R-project.org/> (Vienna, Austria, 2016).
47. Marcel, M. Cutadapt removes adapter sequences from high-throughput sequencing reads. *EMBnet journal* **17**, 10–12 (2011).
48. Kim, D. *et al.* TopHat2: accurate alignment of transcriptomes in the presence of insertions, deletions and gene fusions. *Genome Biol.* **14**, R36 (2013).
49. Anders, S., Pyl, P. T. & Huber, W. HTSeq—a Python framework to work with high-throughput sequencing data. *Bioinformatics* **31**, 166–169 (2015).
50. Love, M. I., Huber, W. & Anders, S. Moderated estimation of fold change and dispersion for RNA-seq data with DESeq2. *Genome Biol.* **15**, 550 (2014).
51. Bao, X. R. *et al.* Mitochondrial dysfunction remodels one-carbon metabolism in human cells. *eLife* **5**, e10575 (2016).
52. Mayr, J. A. *et al.* Mitochondrial phosphate-carrier deficiency: a novel disorder of oxidative phosphorylation. *Am. J. Hum. Genet.* **80**, 478–484 (2007).
53. Langmead, B. & Salzberg, S. L. Fast gapped-read alignment with Bowtie 2. *Nat. Methods* **9**, 357–359 (2012).
54. Ramírez, F. *et al.* deepTools2: a next generation web server for deep-sequeencing data analysis. *Nucleic Acids Res.* **44** (W1), W160–W165 (2016).
55. Garrison, E. & Marth, G. Haplotype-based variant detection from short-read sequencing. Preprint at <https://arxiv.org/abs/1207.3907> (2012).
56. Hahne, F. & Ivanek, R. Visualizing genomic data using Gviz and Bioconductor. *Methods Mol. Biol.* **1418**, 335–351 (2016).
57. Ingolia, N. T., Brar, G. A., Rouskin, S., McGeachy, A. M. & Weissman, J. S. The ribosome profiling strategy for monitoring translation in vivo by deep sequencing of ribosome-protected mRNA fragments. *Nat. Protocols* **7**, 1534–1550 (2012).
58. Rooijers, K., Loayza-Puch, F., Nijtmans, L. G. & Agami, R. Ribosome profiling reveals features of normal and disease-associated mitochondrial translation. *Nat. Commun.* **4**, 2886 (2013).
59. Couvillion, M. T., Soto, I. C., Shipkovenka, G. & Churchman, L. S. Synchronized mitochondrial and cytosolic translation programs. *Nature* **533**, 499–503 (2016).
60. Dunn, J. G. *plastid: a positional library for sequencing analysis*; <http://plastid.readthedocs.io> (2016).
61. Nakahigashi, K. *et al.* Effect of codon adaptation on codon-level and gene-level translation efficiency in vivo. *BMC Genomics* **15**, 1115 (2014).
62. Balakrishnan, R., Oman, K., Shoji, S., Bundschuh, R. & Fredrick, K. The conserved GTPase LepA contributes mainly to translation initiation in *Escherichia coli*. *Nucleic Acids Res.* **42**, 13370–13383 (2014).
63. Oh, E. *et al.* Selective ribosome profiling reveals the cotranslational chaperone action of trigger factor in vivo. *Cell* **147**, 1295–1308 (2011).
64. Dunn, J. G., Foo, C. K., Bellefleur, N. G., Gavis, E. R. & Weissman, J. S. Ribosome profiling reveals pervasive and regulated stop codon readthrough in *Drosophila melanogaster*. *eLife* **2**, e01179 (2013).
65. Wang, Y., Geer, L. Y., Chappay, C., Kans, J. A. & Bryant, S. H. Cn3D: sequence and structure views for Entrez. *Trends Biochem. Sci.* **25**, 300–302 (2000).
66. Krogh, A., Larsson, B., von Heijne, G. & Sonnhammer, E. L. Predicting transmembrane protein topology with a hidden Markov model: application to complete genomes. *J. Mol. Biol.* **305**, 567–580 (2001).

67. Del Campo, C., Bartholomäus, A., Fedyunin, I. & Ignatova, Z. Secondary structure across the bacterial transcriptome reveals versatile roles in mRNA regulation and function. *PLoS Genet.* **11**, e1005613 (2015).
68. Danson, M. J. & Hough, D. W. Citrate synthase from hyperthermophilic Archaea. *Methods Enzymol.* **331**, 3–12 (2001).
69. Feichtinger, R. G. *et al.* Low aerobic mitochondrial energy metabolism in poorly- or undifferentiated neuroblastoma. *BMC Cancer* **10**, 149 (2010).
70. Rustin, P. *et al.* Biochemical and molecular investigations in respiratory chain deficiencies. *Clin. Chim. Acta* **228**, 35–51 (1994).
71. Clayton, D. A. & Shadel, G. S. Isolation of mitochondria from tissue culture cells. *Cold Spring Harb. Protoc.* <http://doi.org/10.1101/pdb.prot080002> (2014).
72. Zheng, G. *et al.* ALKBH5 is a mammalian RNA demethylase that impacts RNA metabolism and mouse fertility. *Mol. Cell* **49**, 18–29 (2013).
73. Ogata, T. *et al.* Chemical synthesis and properties of 5-taurinomethyluridine and 5-taurinomethyl-2-thiouridine. *J. Org. Chem.* **74**, 2585–2588 (2009).
74. Shevchenko, A., Tomas, H., Havlis, J., Olsen, J. V. & Mann, M. In-gel digestion for mass spectrometric characterization of proteins and proteomes. *Nat. Protocols* **1**, 2856–2860 (2006).
75. Dorfer, V. *et al.* MS Amanda, a universal identification algorithm optimized for high accuracy tandem mass spectra. *J. Proteome Res.* **13**, 3679–3684 (2014).
76. Eng, J. K., McCormack, A. L. & Yates, J. R. An approach to correlate tandem mass spectral data of peptides with amino acid sequences in a protein database. *J. Am. Soc. Mass Spectrom.* **5**, 976–989 (1994).
77. Bern, M., Kil, Y. J. & Becker, C. Byonic: advanced peptide and protein identification software. *Curr. Protoc. Bioinformatics* **Chapter 13**, Unit13.20 (2012).
78. Spivak, M., Weston, J., Bottou, L., Käll, L. & Noble, W. S. Improvements to the percolator algorithm for Peptide identification from shotgun proteomics data sets. *J. Proteome Res.* **8**, 3737–3745 (2009).
79. MacLean, B. *et al.* Skyline: an open source document editor for creating and analyzing targeted proteomics experiments. *Bioinformatics* **26**, 966–968 (2010).
80. Schilling, B. *et al.* Platform-independent and label-free quantitation of proteomic data using MS1 extracted ion chromatograms in skyline: application to protein acetylation and phosphorylation. *Mol. Cell. Proteomics* **11**, 202–214 (2012).
81. Renwick, S. B., Snell, K. & Baumann, U. The crystal structure of human cytosolic serine hydroxymethyltransferase: a target for cancer chemotherapy. *Structure* **6**, 1105–1116 (1998).



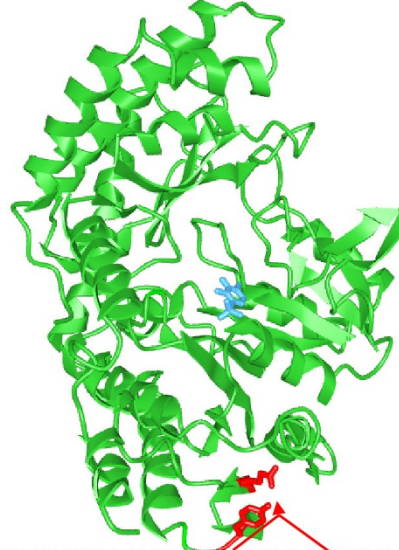
Extended Data Figure 1 | SHMT2 deletion-induced respiratory chain dysfunction in different cellular backgrounds and clones. a, Change in media colour after 48 h cell growth. **b**, **c**, Lactate secretion (**b**) and normalized NAD⁺/NADH ratio (**c**) of HCT116 knockout cell lines ($n = 6$). **d**, **e**, Basal respiration as measured by Seahorse XF analyser ($n = 3$) (**d**) and normalized NAD⁺/NADH ratio ($n = 3$) (**e**) of HEK293T folate 1C gene CRISPR-Cas9 knockout cell lines. **f**, Normalized levels of TCA cycle and associated metabolites ($n = 3$). **g**, Steady-state labelling fraction into citrate

from [U-¹³C] substrates glutamine (left) and glucose (right) ($n = 3$). **h**, Immunoblot of extracted mitochondria for subunits of respiratory chain complexes I-V (CI-CV) and markers of mitochondrial mass. **i**, Mitochondrial complex I levels (NDUFS4) in independent HCT116 folate 1C gene knockout clones. Data are mean \pm s.e.m. n indicates the number of biological replicates. * $P < 0.01$, two-tailed Student's t -test (see Supplementary Table 7 for exact P values).

a SHMT2 pyridoxal phosphate binding deficient mutant
p.Lys280Gln

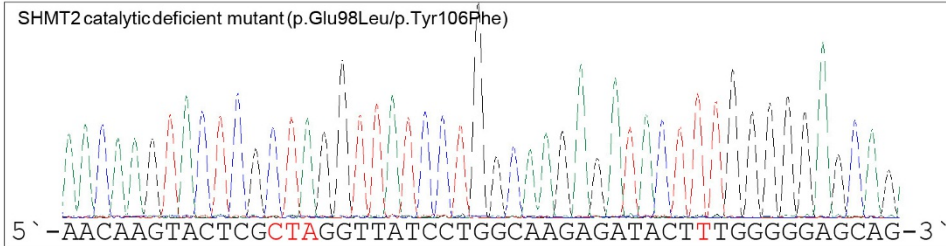


SHMT2 catalytic deficient double mutant
p.Glu98Leu/p.Tyr106Phe

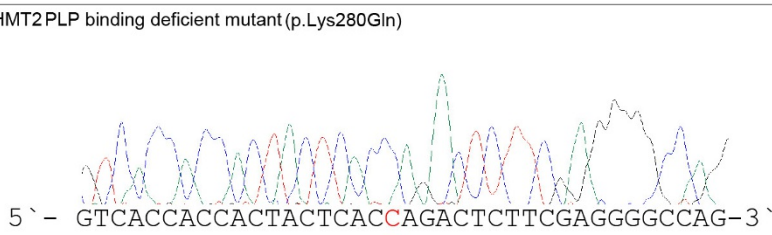


P0A825	GLYA_ECOLI	15	LWCAMEQEKVRCEEHIELTASENYTSPRVMOAQQSOLTNKYAEYYPGKRYYGCCYVDIV	74
P34897	GLYM_HUMAN	56	MWELLQREKDRQCRGLELITASENFCRAALEALGSCLNKYSSEYPGKRYYGAFAVVDEI	115
P34896	GLYC_HUMAN	33	VYNIKKESNRORVGLELIASENFASRAVLEALGSCLNKYSSEYPGORYYGTTEFIDEL	92
			::: ::*: ** :*****: * : * * * :*****: * * : * * :	
P0A825	GLYA_ECOLI	75	EQLAIDRAKELFGADY----ANVOPHSSQANFAVYTALLEPGDVTLGMNLAHGGHLTHG	130
P34897	GLYM_HUMAN	116	ELLQRRALEAFDLDPAQWGVNVOPYSGSPANLAVYTALLOPHDRIMGLDLPDGGHLTHG	175
P34896	GLYC_HUMAN	93	ETLCQKRRLQAYKLDPCWGVNVOPYSGSPANFAVYTALVEPHGRIMGLDLPDGGHLTHG	152
			* * * ** : * : *	
P0A825	GLYA_ECOLI	131	SPVN-----FSGKLYNIVPYGID-ATGHIDYADLEKQKAKEHKPKMIICGFSAYSQVVDWA	184
P34897	GLYM_HUMAN	176	YMSDVKRISATSIFFESMPYKLNPKTGLIDYNCLALTALEFRPLIIAGTSAVARLIDYA	235
P34896	GLYC_HUMAN	153	FMTDKKKISATSIFFESMPYKVNPDTCYINVDLEENARLEPHKLIITAGTSCYSRNLEYA	212
			:: : *	
P0A825	GLYA_ECOLI	185	KMREIADSIGAYLFDVMAHVAGLVAAGVYENVPVPHAHVVTTTTHKTLRAGPRGGLIAKGG	244
P34897	GLYM_HUMAN	236	RMREVCDEVKAHLADMAHISGLVAARVIPSFFKHADIVTTTTHKTLRAGRSGLIFYRKG	295
P34896	GLYC_HUMAN	213	RLRKIADENGAYLMADMAHISGLVAAGVVPSEFFCHVVTVTTHKTLRGCRAGMIFYRKG	272
			::*:*: *	

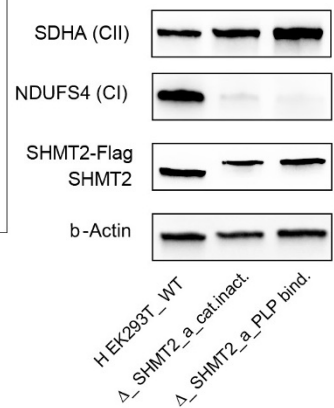
b SHMT2 catalytic deficient mutant (p.Glu98Leu/p.Tyr106Phe)



SHMT2 PLP binding deficient mutant (p.Lys280Gln)

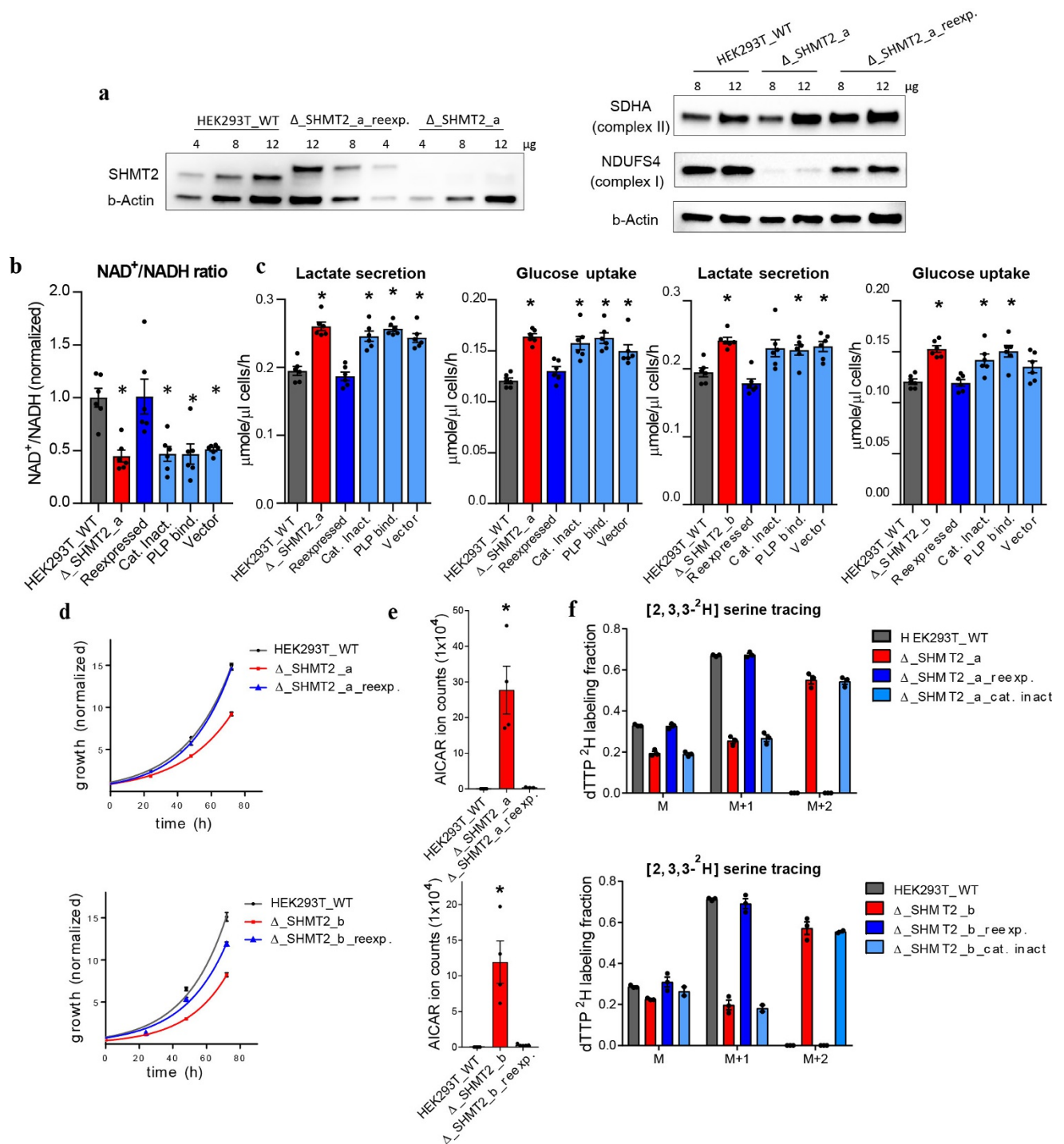


c



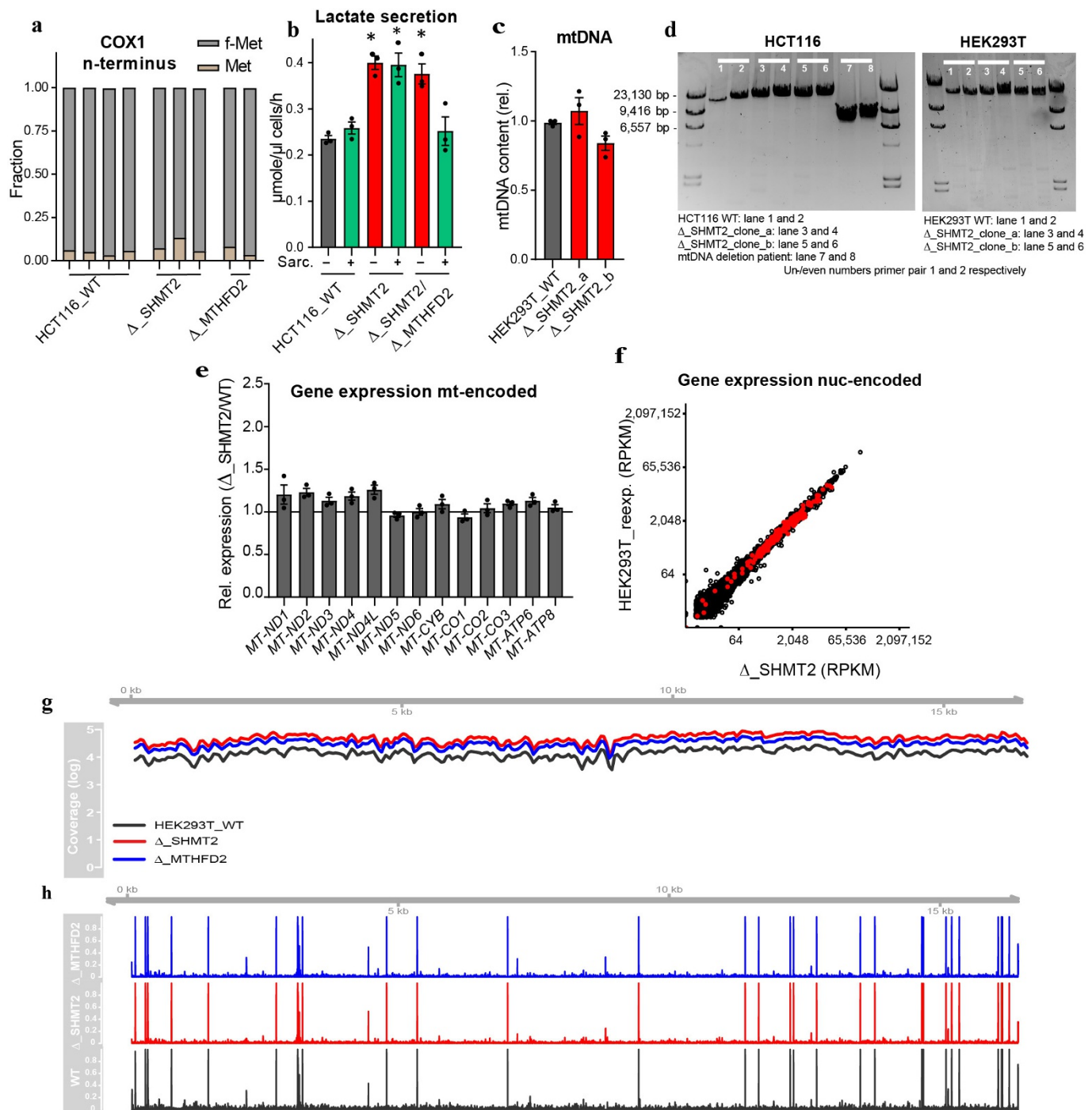
Extended Data Figure 2 | Catalytically deficient SHMT2 constructs. **a**, Mapping of mutated amino acid residues on human SHMT1 (PDB code 1Bj4⁸¹) using iCn3D and alignment of *E. coli* serine hydroxymethyltransferase (GLYA), *H. sapiens* mitochondrial serine hydroxymethyltransferase 2 (GLYM) and cytosolic serine

hydroxymethyltransferase 1 (GLYC). Positions for GLYM are given with reference to GenBank NM_005412.5. **b**, Sanger sequencing traces of mutant constructs. **c**, Immunoblot for mitochondrial complex I levels (NDUFS4) in cell lines re-expressing catalytically deficient forms of SHMT2.



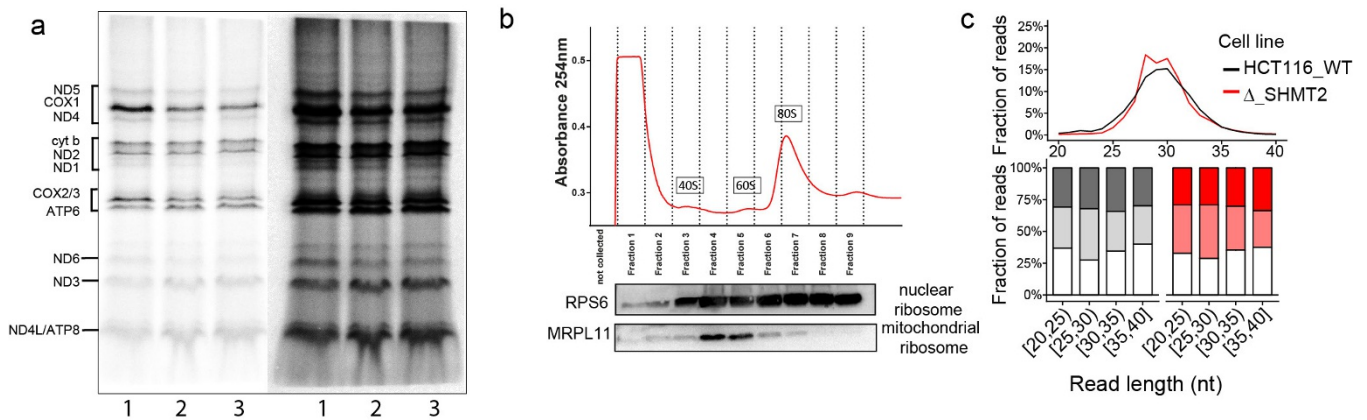
Extended Data Figure 3 | Restoring SHMT2 catalytic activity normalizes 1C flux, respiratory chain expression, glycolytic activity, and cell growth. **a**, Immunoblot of re-expression of catalytically active SHMT2 (left) and the effects of its re-expression on mitochondrial complex I and II levels (right). **b–f**, Effect of re-expression of catalytically active and inactive forms of SHMT2 in two different Δ SHMT2 clones in the HEK293T background. **b**, Normalized NAD^+/NADH ratio ($n=6$). **c**, Lactate secretion and glucose uptake ($n=6$). **d**, Cell proliferation

($n=6$). **e**, Purine biosynthesis intermediate 5-aminoimidazole-4-carboxamide ribonucleotide (AICAR) levels ($n=4$) as an indicator of cytosolic folate 1C status. **f**, $[2,3,3\text{-}^2\text{H}]$ serine tracing to differentiate cytosolic from mitochondrial folate 1C unit production for incorporation into deoxythymidine triphosphate ($n=3$). Data are mean \pm s.e.m. n indicates the number of biological replicates. $*P < 0.01$, two-tailed Student's t -test (see Supplementary Table 7 for exact P values).



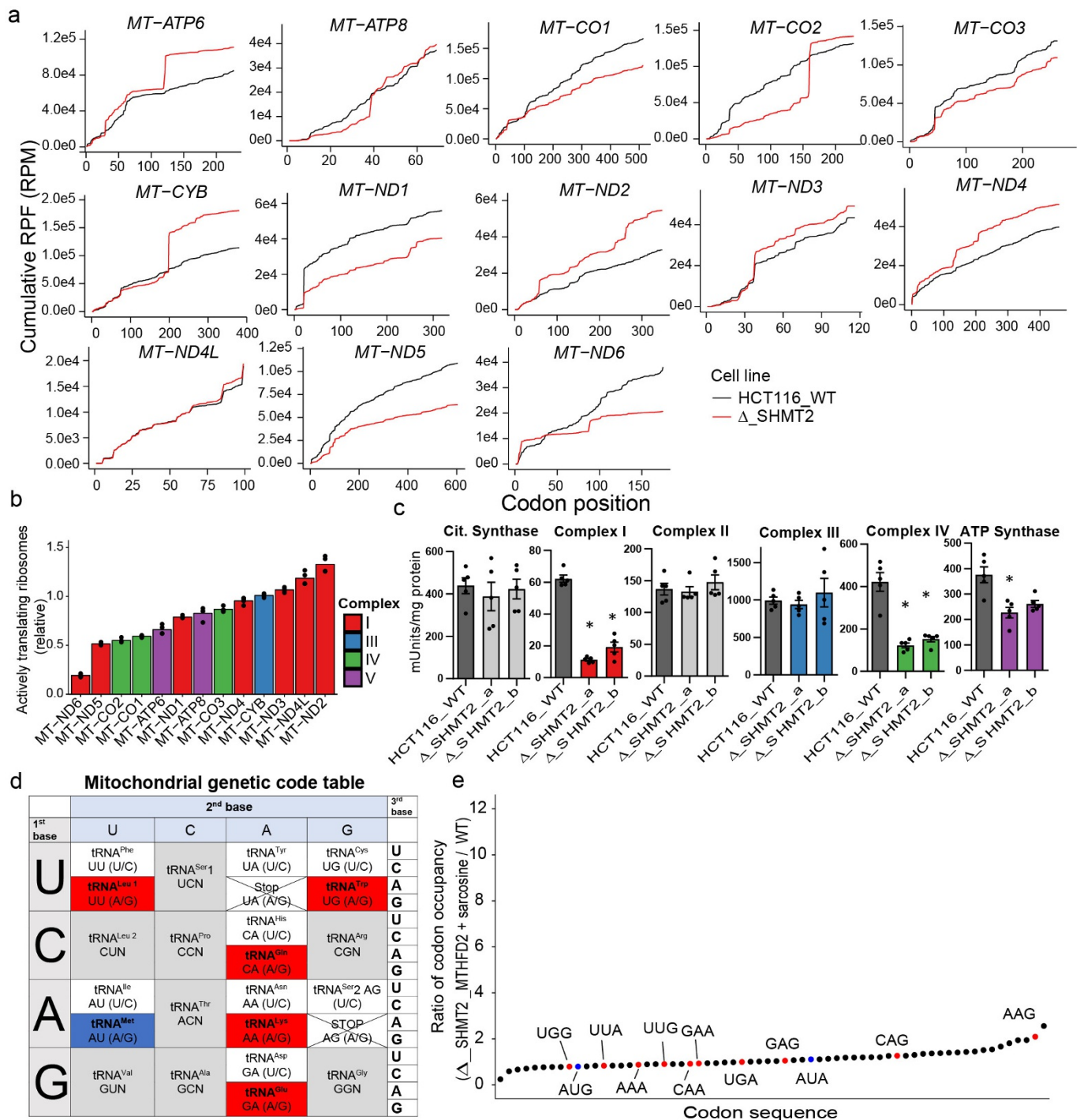
Extended Data Figure 4 | Oxidative phosphorylation defect is caused by a post-transcriptional mechanism independent of methionine formulation. **a**, Fraction of initiating amino acid (formylmethionine versus methionine) of mitochondrial-expressed COX1 peptide determined by high-resolution LC-MS (wild type $n = 4$, Δ SHMT2 $n = 3$, Δ MTHFD2 $n = 2$). **b**, Lactate secretion ($n = 3$) upon sarcosine supplementation (1 mM). **c**, Relative mtDNA levels in HEK293T cells ($n = 3$). **d**, Agarose gel of mtDNA long-range PCR products of HCT116 and HEK293T knockout cell lines. **e**, Relative mRNA levels of mtDNA-encoded respiratory chain subunits in the HEK293T background ($n = 3$). **f**, Gene expression levels in SHMT2-knockout cell lines compared to SHMT2 wild-type re-expressed

lines by total RNA sequencing. Each dot represents mean gene expression as derived from two biological replicates of two independent knockout clones and matched re-expressed lines ($n = 4$). Genes linked to human OXPHOS function³⁷ are highlighted in red. Significantly differentially expressed genes are listed in Supplementary Table 2. **g**, Position-dependent next-generation sequencing coverage of mtDNA in HEK293T wild-type, SHMT2-knockout and MTHFD2-knockout cell lines supports the absence of deletions due to SHMT2 loss. **h**, Corresponding variant position and frequency. Variant list is provided in Supplementary Table 1. Data are mean \pm s.e.m. n indicates the number of biological replicates. $*P < 0.01$, two-tailed Student's t -test (see Supplementary Table 7 for exact P values).



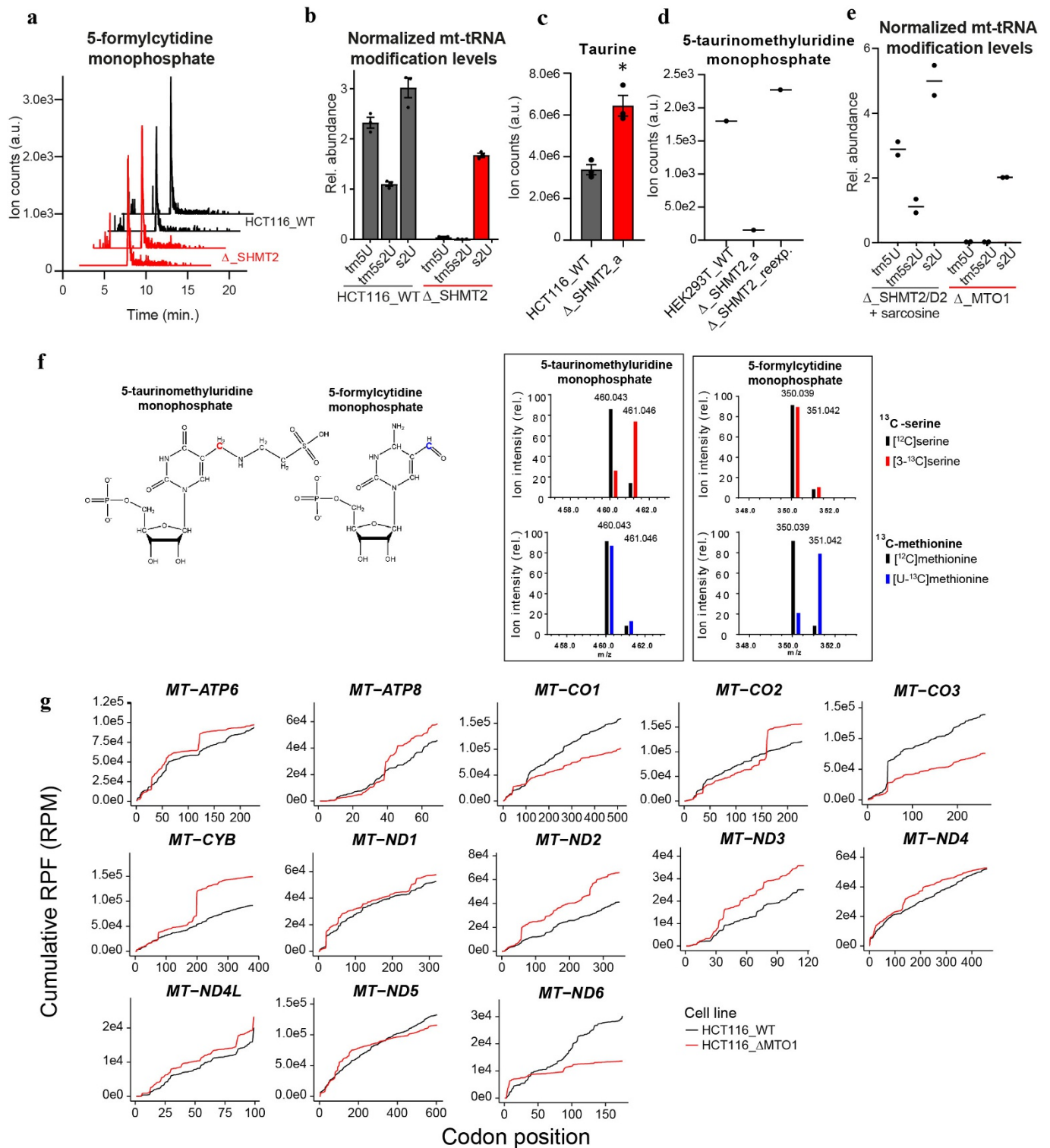
Extended Data Figure 5 | Impairment of mitochondrial translation due to loss of SHMT2. **a**, SDS-PAGE of [35 S]methionine-labelled mitochondrially translated proteins in wild-type (lane 1) and two SHMT2-knockout (lane 2 and 3) HEK293T cell lines. Decreased synthesis of COX1 and COX2/3 are evident upon short exposure and reduced synthesis of ND5 and ND6 is more easily visualized upon longer exposure. **b**, Absorbance at 254 nm upon sucrose gradient fractionation of cell lysates digested by micrococcal nuclease (Fig. 3a). Fractions corresponding to 4

and 5 were collected for mitochondrial ribosome enrichment as shown on the matched immunoblot for mitochondrial ribosome subunit MRPL11. **c**, Read length distribution (top) and read length-dependent sub-codon read phasing (bottom) across the 13 mitochondrial protein-coding transcripts. Data in **c** are based on the mitochondrial ribosome profiling experiment in Fig. 3, and represent the mean of two technical replicates of two independent samples.



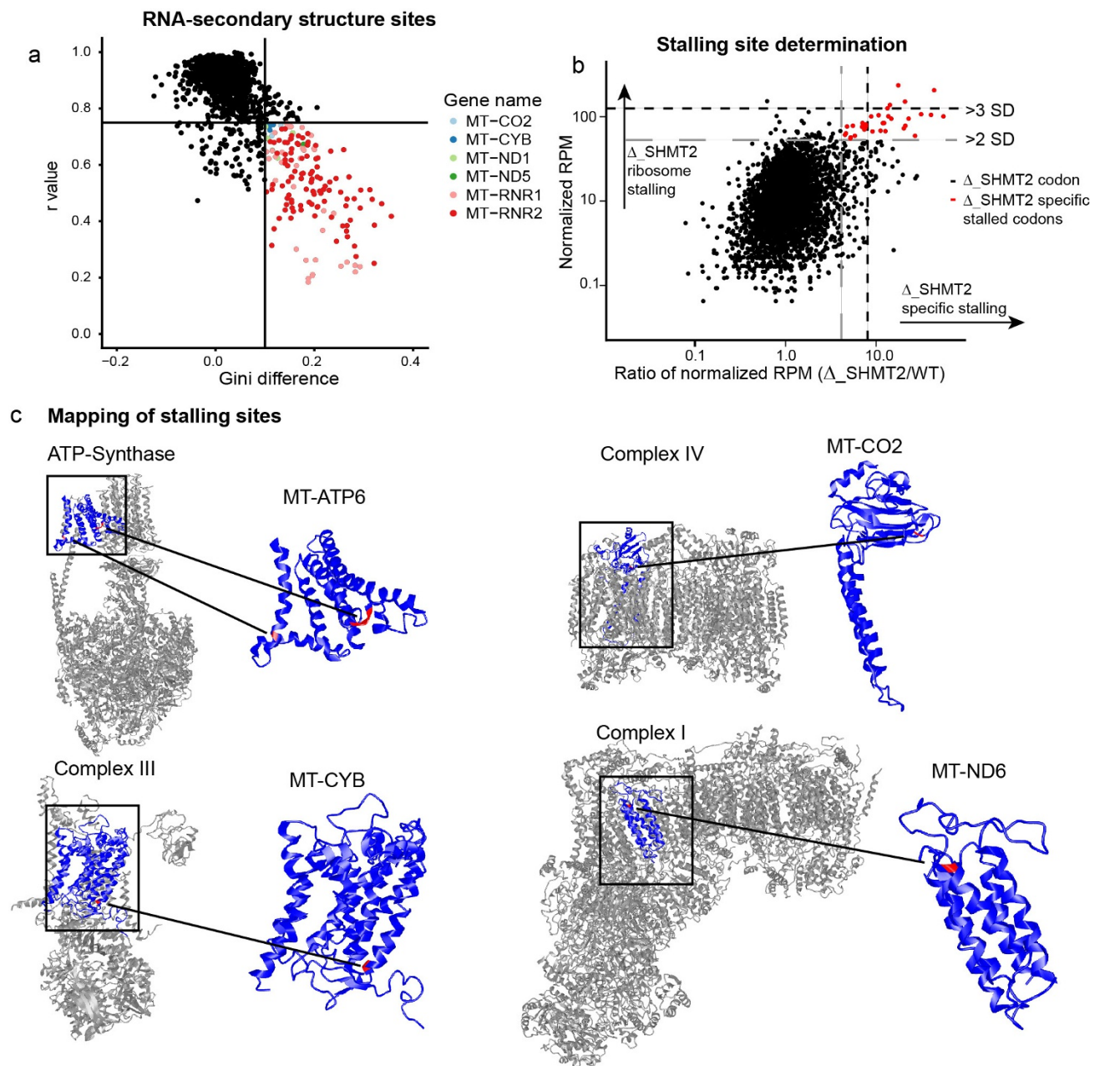
Extended Data Figure 6 | Mitochondrial ribosome stalling at guanosine-ending split codon box nucleotide triplets suggests deficient 5-taurinomethyluridine modification. **a**, Expanded version of Fig. 3b, showing the mean cumulative ribosome protected fragments of all mitochondrial protein-coding genes. **b**, Mean relative density of actively translating (that is, not stalled) ribosomes for mitochondrial transcripts. Data in **a** and **b** represent two technical replicates of two independent samples. **c**, Enzymatic activities of citrate synthase and individual mitochondrial respiratory chain complexes from mitochondrial extracts ($n = 5$). Data are mean \pm s.e.m. * $P < 0.01$, two-tailed Student's t -test

(see Supplementary Table 7 for exact P values). **d**, Mitochondrial genetic code table with split codon boxes depending on taurinomethylated tRNAs for translation highlighted in red. Codons decoded by anticodon formylcytidine-containing tRNA^{Met} are highlighted in blue. **e**, Mean codon-specific mitochondrial ribosome occupancy of HCT116 SHMT2/MTHFD2 double-knockout cell lines supplemented with sarcosine (1 mM). Codons highlighted in red are decoded by tRNAs carrying a 5-taurinomethyluridine modification. The supplementation with sarcosine prevents the stalling normally observed with SHMT2 deletion ($n = 2$).



Extended Data Figure 7 | tRNA modification status in Δ SHMT2 and effects of 5-taurinomethyluridine modification loss caused by human disease gene MTO1. a, Total ion chromatogram of 5-formylcytidine monophosphate in digested mitochondrial tRNAs upon loss of SHMT2. The same samples were analysed for 5-taurinomethyluridine monophosphate (p- τ m⁵U) in Fig. 4b. The combined data demonstrate that SHMT2 deletion causes loss of τ m⁵U but not 5-formylcytidine. **b**, Levels of τ m⁵U, 5-taurinomethyl-2-thiouridine monophosphate (p- τ m⁵s²U) and 2-thiouridine monophosphate (p-s²U) in wild-type HCT116 and SHMT2 deletion lines normalized to 5-formylcytidine monophosphate (p-f⁵C) ($n=3$). **c**, Taurine levels in HCT116 wild-type and SHMT2-knockout cells ($n=3$). **d**, τ m⁵U levels in digested mitochondrial tRNAs upon

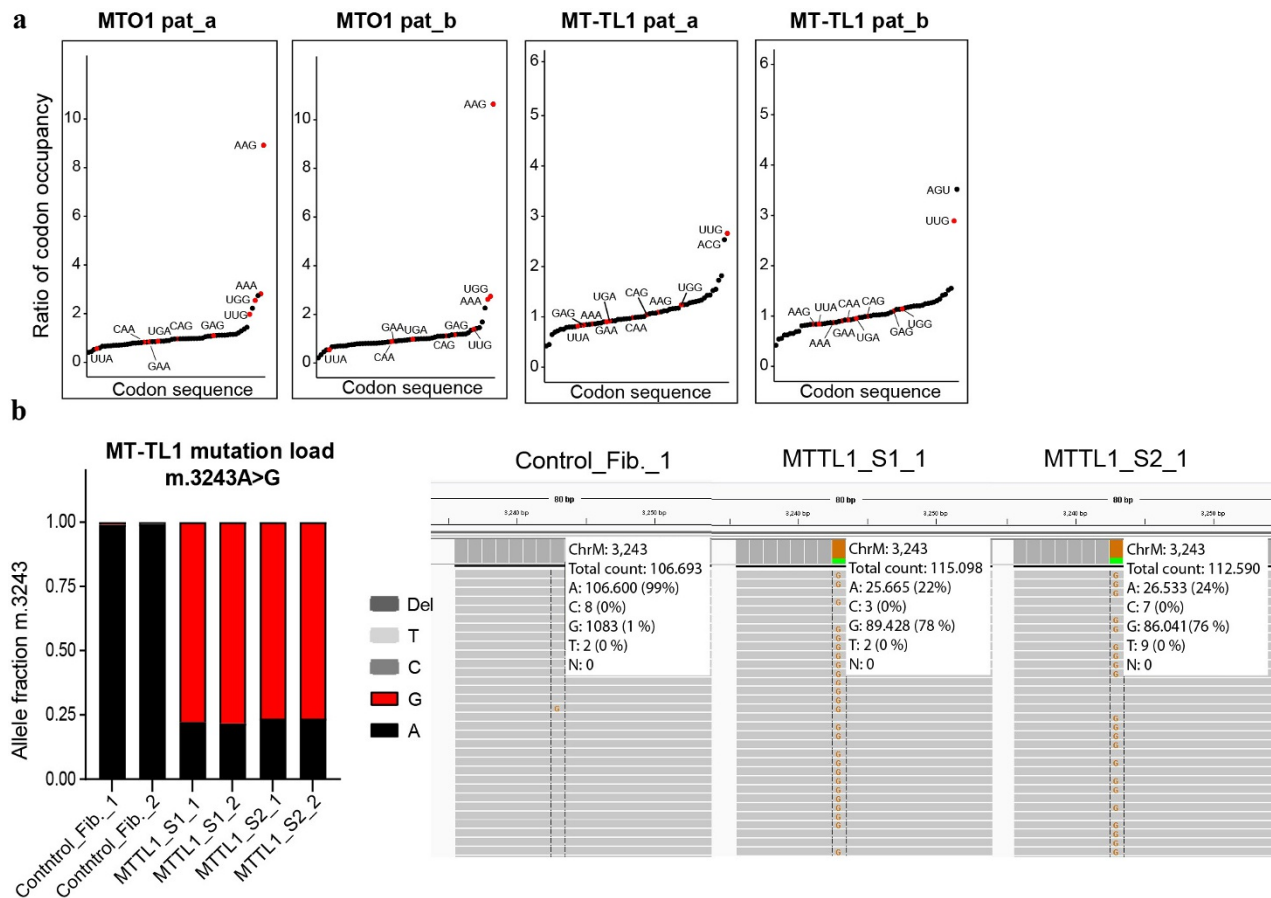
re-expression of SHMT2 ($n=1$). **e**, τ m⁵U, τ m⁵s²U and s²U levels normalized to f⁵C in HCT116 SHMT2/MTHFD2 knockout lines after sarcosine supplementation and HCT116 upon loss of MTO1 ($n=2$). For all panels, data are mean \pm s.e.m. or individual data points only. **f**, Labelling pattern of 5-taurinomethyluridine and 5-formylcytidine monophosphate extracted from mitochondrial tRNAs after growth in media containing either [3-¹³C]serine or [U-¹³C]methionine. **g**, Mean cumulative count of ribosome protected fragments (RPF) mapping to mitochondrial protein coding transcripts upon ribosome profiling in HCT116 MTO1-knockout cell lines. Data were normalized to RPM ($n=2$); n indicates the number of biological replicates. * $P < 0.01$, two-tailed Student's t -test (see Supplementary Table 7 for exact P values).



Extended Data Figure 8 | Investigation of mRNA and protein secondary structure effects on mitochondrial ribosome stalling sites.

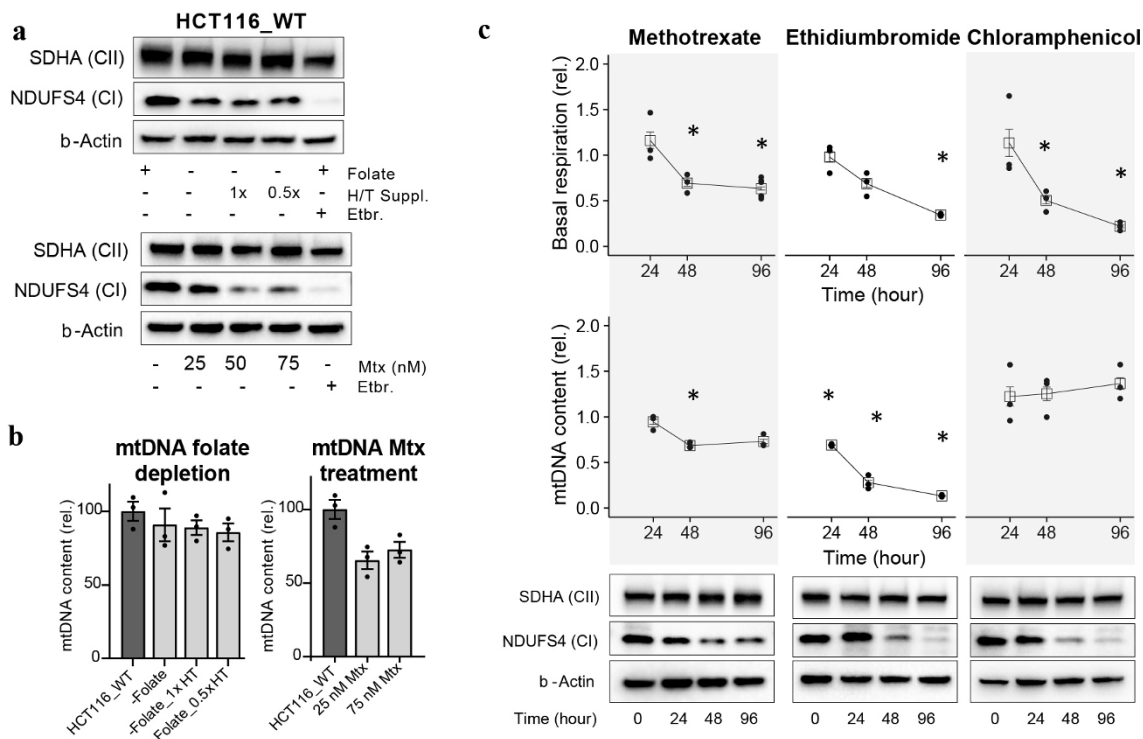
a, Identification of mitochondrial RNA secondary structure based on analysis of the mitochondrial transcript data from the dimethyl sulfate sequencing dataset published previously³⁴. *R* values and Gini differences were calculated to detect changes in nucleotide reactivity between the *in vivo* and denatured condition for the complete mitochondrial transcriptome. Coloured points indicate structured regions given in Supplementary Table 4. **b**, Determination of ribosome stalling sites in SHMT2-knockout HCT116 cell lines. Data points represent individual codons of all 13 mitochondrial protein-coding transcripts. For each codon,

the *y* axis indicates the ribosome counts normalized to the gene median in RPM. The *x* axis indicates the ratio of normalized counts in SHMT2-knockout to normalized counts in wild-type HCT116. Two and three s.d. above the mean of all codons in the genome are indicated by the grey and black dotted line, respectively. Highlighted in red are codons with greater than 2 s.d. **c**, Mapping of AAG and UUG codons from SHMT2 knockout-specific ribosome stalling sites (>3 s.d.) on protein structures. For **b** and **c**, analysis is based on ribosome profiling data in Fig. 3, with two technical replicates of two independent samples. A list of identified codons and mapped AAG and UUG sites is provided in Supplementary Table 5.



Extended Data Figure 9 | Mitochondrial transcript codon occupancy from ribosome profiling of individual patient lines. **a**, Codon-specific mitochondrial ribosome occupancy ratio (patient/control fibroblasts) in individual patient derived cell lines ($n=1$ for each individual patient, normalized to mean of $n=2$ control fibroblast lines). Patients either had nuclear *MTO1* missense mutations (patient A c.[1261-5T>G];[1430G>A], patient B c.[1222T>A];[1222T>A]) or were diagnosed with MELAS and

carry the recurrent point mutation m.3243A>G in the mitochondrial gene for tRNA Leu1 (*MT-TL1*). **b**, Next-generation sequencing of mtDNA mutation load m.3243A>G (*MT-TL1*) in control fibroblasts and MELAS patient cell lines. Each bar shows one biological replicate for control and patient cell lines. Integrative genomics viewer sequencing raw data are shown on the right.



Extended Data Figure 10 | Effects of targeting 1C metabolism on mitochondrial function. **a**, Mitochondrial complex I and II levels after growth in the absence of folate for five passages or in the presence of the indicated methotrexate concentration for 96 h. Ethidium bromide (250 nM) was used as a positive control. **b**, Cellular mtDNA levels in HCT116 cells after folate depletion (with or without 100 μ M hypoxanthine and 16 μ M thymidine (HT) as rescue agents) or in the presence of methotrexate for 96 h ($n = 3$). **c**, To determine whether the decrease in respiration due to methotrexate arises from methotrexate depleting mitochondrial DNA, impairing mitochondrial translation, or a combination, in HCT116 cells we compared the effects of methotrexate (50 nM) to ethidium bromide (250 nM = 100 ng ml⁻¹), which is

classically used to deplete mitochondrial DNA, and to chloramphenicol (310 μ M = 100 μ g ml⁻¹), which blocks mitochondrial translation. After 48 h of treatment, methotrexate and ethidium bromide both decreased oxygen consumption and DNA content. Importantly, despite ethidium bromide depleting mitochondrial DNA much more strongly, methotrexate had an equivalent effect on oxygen consumption, consistent with the effect of methotrexate on oxygen consumption being in part via mitochondrial translation inhibition. Data are normalized and compared to untreated control (all $n = 3$; except oxygen consumption methotrexate 96 h $n = 6$ and control $n = 4$). Data are mean \pm s.e.m. n indicates the number of biological replicates. * $P < 0.01$, two-tailed Student's t -test (see Supplementary Table 7 for exact P values).

Life Sciences Reporting Summary

Nature Research wishes to improve the reproducibility of the work that we publish. This form is intended for publication with all accepted life science papers and provides structure for consistency and transparency in reporting. Every life science submission will use this form; some list items might not apply to an individual manuscript, but all fields must be completed for clarity.

For further information on the points included in this form, see [Reporting Life Sciences Research](#). For further information on Nature Research policies, including our [data availability policy](#), see [Authors & Referees](#) and the [Editorial Policy Checklist](#).

▶ Experimental design

1. Sample size

Describe how sample size was determined.

No statistical methods were used to predetermine sample size. Sample size was based on experimental feasibility, sample availability, and N necessary to obtain definitive results.

2. Data exclusions

Describe any data exclusions.

None.

3. Replication

Describe whether the experimental findings were reliably reproduced.

Experimental findings were successfully replicated at least twice.

4. Randomization

Describe how samples/organisms/participants were allocated into experimental groups.

Samples were allocated into experimental groups by the confirmed genetic modification of the cell line they were derived from (CRISPR/Cas9 deletion) or the respective drug treatment. This design does not allow for randomization, as the origin of samples is critical. However, whenever possible samples were analyzed in a randomized order (i.e. when run on liquid-chromatography mass spectrometry).

5. Blinding

Describe whether the investigators were blinded to group allocation during data collection and/or analysis.

This study did not involve animals or human research participants. The researchers were not blinded during data collection and/or analysis.

Note: all studies involving animals and/or human research participants must disclose whether blinding and randomization were used.

6. Statistical parameters

For all figures and tables that use statistical methods, confirm that the following items are present in relevant figure legends (or in the Methods section if additional space is needed).

n/a Confirmed

- The exact sample size (n) for each experimental group/condition, given as a discrete number and unit of measurement (animals, litters, cultures, etc.)
- A description of how samples were collected, noting whether measurements were taken from distinct samples or whether the same sample was measured repeatedly
- A statement indicating how many times each experiment was replicated
- The statistical test(s) used and whether they are one- or two-sided (note: only common tests should be described solely by name; more complex techniques should be described in the Methods section)
- A description of any assumptions or corrections, such as an adjustment for multiple comparisons
- The test results (e.g. P values) given as exact values whenever possible and with confidence intervals noted
- A clear description of statistics including central tendency (e.g. median, mean) and variation (e.g. standard deviation, interquartile range)
- Clearly defined error bars

See the web collection on [statistics for biologists](#) for further resources and guidance.

► Software

Policy information about [availability of computer code](#)

7. Software

Describe the software used to analyze the data in this study.

The following software was used to analyze data in our study:

Next-Generation sequencing raw data was processed using the Galaxy system with software-packages and version numbers given below:

Cutadapt (Galaxy version 1.6)
TopHat (Galaxy Version 0.9)
htseq-count (Galaxy Version 0.6.1galaxy1)
Bowtie2 (Galaxy Version 0.6)
DeepTools bamCoverage (Galaxy Version 2.3.6.0)
Freebayes (Galaxy Version 0.4.1)
BWA (Galaxy Version 0.9)

Ribosome profiling data was additionally processed using scripts from the plastid package version 0.4.8

For downstream analysis R the software for statistical computing was used (Version 3.3.1) with software-packages and version numbers given below:

DESeq2 package (Version 1.12.3)
Gviz package (Version 1.18.0)
dplyr (Version 0.5.0)
ggplot (Version 2 2.2.1)
tibble (Version 1.2)
tidyr (Version 0.6.1)

Data from high resolution mass-spectrometry was analyzed using the Metabolomic Analysis and Visualization Engine (MAVEN build 682)

Small scale data was processed using GraphPad Prism 7.02.

For manuscripts utilizing custom algorithms or software that are central to the paper but not yet described in the published literature, software must be made available to editors and reviewers upon request. We strongly encourage code deposition in a community repository (e.g. GitHub). *Nature Methods* [guidance for providing algorithms and software for publication](#) provides further information on this topic.

► Materials and reagents

Policy information about [availability of materials](#)

8. Materials availability

Indicate whether there are restrictions on availability of unique materials or if these materials are only available for distribution by a for-profit company.

There are no restrictions on availability of materials used in this study.

9. Antibodies

Describe the antibodies used and how they were validated for use in the system under study (i.e. assay and species).

Antibodies were used in according to the manufacturer's directions. Antibodies against folate 1C enzymes used in this study were cross-validated in this study by the loss of the specific band in sequence verified CRISPR/Cas9 knockout cell lines.

Antibodies used from Cell Signaling:
Anti-SHMT1 (12612; Lot: 01/2017): validated for immunoblotting by provider; validated for use in human samples; references: PMID:27307216; PMID: 27110680; validated by CRISPR/Cas9 knockout
Anti-SHMT2 (12762; Lot:07/2016): validated for immunoblotting by provider; validated for use in human samples; references: PMID: 27604570; PMID: 27126896; validated by CRISPR/Cas9 knockout
Anti-MRPL11 (2066; Lot: 09/2015): validated for immunoblotting by provider; validated for use in human samples; reference: PMID: 22829971;
Anti-S6RP (5G10; Lot: 08/2015): validated for immunoblotting by provider; validated for use in human samples; references: PMID: 28367235, PMID: 28348518
Anti- β -actin HRP (5125; Lot: 04/2016): validated for immunoblotting by provider; validated for use in human samples; references: PMID: 28358054, PMID: 27649272

Antibodies used from Abcam Inc.:
Anti-MTHFD2 (ab151447; GR145284-1): validated for immunoblotting by provider; validated for use in human samples; references: PMID: 27732838; validated by CRISPR/Cas9 knockout
Anti-NDUFS4 (ab139178; Lot: YJ052508CS): validated for immunoblotting by provider; validated for use in human samples; reference: PMID: 26053068; knockout validated by supplier
Anti-SDHA (ab14715; Lot: GR192960-6): validated for immunoblotting by provider; validated for use in human samples; references: PMID: 27392540, PMID: 27974379
Anti-SDHB (ab14714; Lot: L6978): validated for immunoblotting by provider; validated for use in human samples; references: PMID: 28414270, PMID: 27345149
Anti-VDAC1 (ab14734; Lot: GR183548-26): validated for immunoblotting by provider; validated for use in human samples; references: PMID: 27974379, PMID: 28028439
Anti-ND1 (ab222892; Lot: GR3184720-1): validated for immunoblotting by provider; validated for use in human samples
Anti-NDUFB8 (ab110242; Lot: L6978): validated for immunoblotting by provider; validated for use in human samples; references: PMID: 28414270, PMID: 27345149
Anti-NDUFS3 (ab110246; Lot: GR255750-5): validated for immunoblotting by provider; validated for use in human samples; references: PMID: 27181046, PMID: 24492964, PMID: 24815183
Anti-CO1 (ab14705; Lot: GR291384-3): validated for immunoblotting by provider; validated for use in human samples; references: PMID: 26971449, PMID: 27828948
Anti-CO2 (ab200615; GR219672-1): validated for immunoblotting by provider; validated for use in human samples
Anti-COX4 (ab14744; GR281421-5): validated for immunoblotting by provider; validated for use in human samples; references: PMID: 21444675; PMID: 20805355
Anti-ATP5A (ab176569; GR303070-2): validated for immunoblotting by provider; validated for use in human samples; references: PMID: 28426667, PMID: 27590850
Anti-mtTFA (ab176558; GR137920-5): validated for immunoblotting by provider; validated for use in human samples; references: PMID: 25561980, PMID: 28714949

Antibodies used from Sigma-Aldrich:
Anti-MTHFD1L (HPA029041; Lot: R31922): verified and developed by Atlas Antibodies; validated for use in human samples; validated by CRISPR/Cas9 knockout
Anti-ND6 (SAB2108622; Lot: QC48692): validated for immunoblotting by provider; validated for use in human samples
Anti-CYB (HPA068400; Lot: R100268): verified and developed by Atlas Antibodies; validated for use in human samples
Anti-UQCRC2 (HPA019146; Lot: R08218): verified and developed by Atlas Antibodies; validated for use in human samples; references: PMID 24130818, PMID 23281071

10. Eukaryotic cell lines

a. State the source of each eukaryotic cell line used.

All cell lines were purchased from ATCC. MTO1 and MT-TL1 patient fibroblasts and controls were provided by the Department of Pediatrics, Salzburger Landeskliniken and Paracelsus Medical University, Salzburg.

b. Describe the method of cell line authentication used.

Sequencing to confirm genetic alterations.

c. Report whether the cell lines were tested for mycoplasma contamination.

All cells have been tested negative for mycoplasma contamination.

d. If any of the cell lines used are listed in the database of commonly misidentified cell lines maintained by [ICLAC](#), provide a scientific rationale for their use.

No such cell lines were used.

► Animals and human research participants

Policy information about [studies involving animals](#); when reporting animal research, follow the [ARRIVE guidelines](#)

11. Description of research animals

Provide details on animals and/or animal-derived materials used in the study.

No animals were used.

Policy information about [studies involving human research participants](#)

12. Description of human research participants

Describe the covariate-relevant population characteristics of the human research participants.

MTO1 and MT-TL1 patient fibroblasts and controls were provided by the Department of Pediatrics, Salzburger Landeskliniken and Paracelsus Medical University, Salzburg. Studies with primary human cell lines were approved by the local ethics-committee and informed consent was obtained from all subjects. Genotype of MTO1 deficient patients (GenBank NM_012123.3) was as follows: pat_a c.[1261-5T>G];[1430G>A], (p.[?];[Arg477His]); pat_b c.[1222T>A];[1222T>A], (p.[Ile408Phe]; [Ile408Phe]). Patient MTO1_pat_b has been reported before. Both MELAS patients carried the common MT-TL1 m.3243A>G mutation with the heteroplasmy rate reported in this study. Further description of human research participants:
 MT-TL1 patient 1: sex: m; age at presentation: 2 week; clinical features: cardiomyopathy, muscle weakness; enzymatic phenotype: complex I+IV defect in muscle biopsy
 MT-TL1 patient 2: sex: f; age at presentation: 6 years; clinical features: developmental delay, sensorineural hearing loss, muscle weakness, microcytic anemia, stroke-like episodes; enzymatic phenotype: complex I defect in muscle biopsy
 MTO1 patient 1: sex: f; age at presentation: intrauterine; clinical features: brain cysts at 18th weeks gestation, hypertrophic cardiomyopathy, muscular hypotonia, partial agenesis of corpus calosum, microcephaly, hypertelorism, low set ears; enzymatic phenotype: complex I+IV defect in muscle biopsy
 MTO1 patient: sex: m; age at presentation: 1 day; hypertrophic cardiomyopathy, perinatal asphyxia, severe global developmental delay; enzymatic phenotype: complex I+IV defect in muscle biopsy